Design, manufacturing and testing of a Floating Wind Turbine

Floating Wind University Challenge

ABCD1234: The 0 ECTS course

The Unsinkable 8

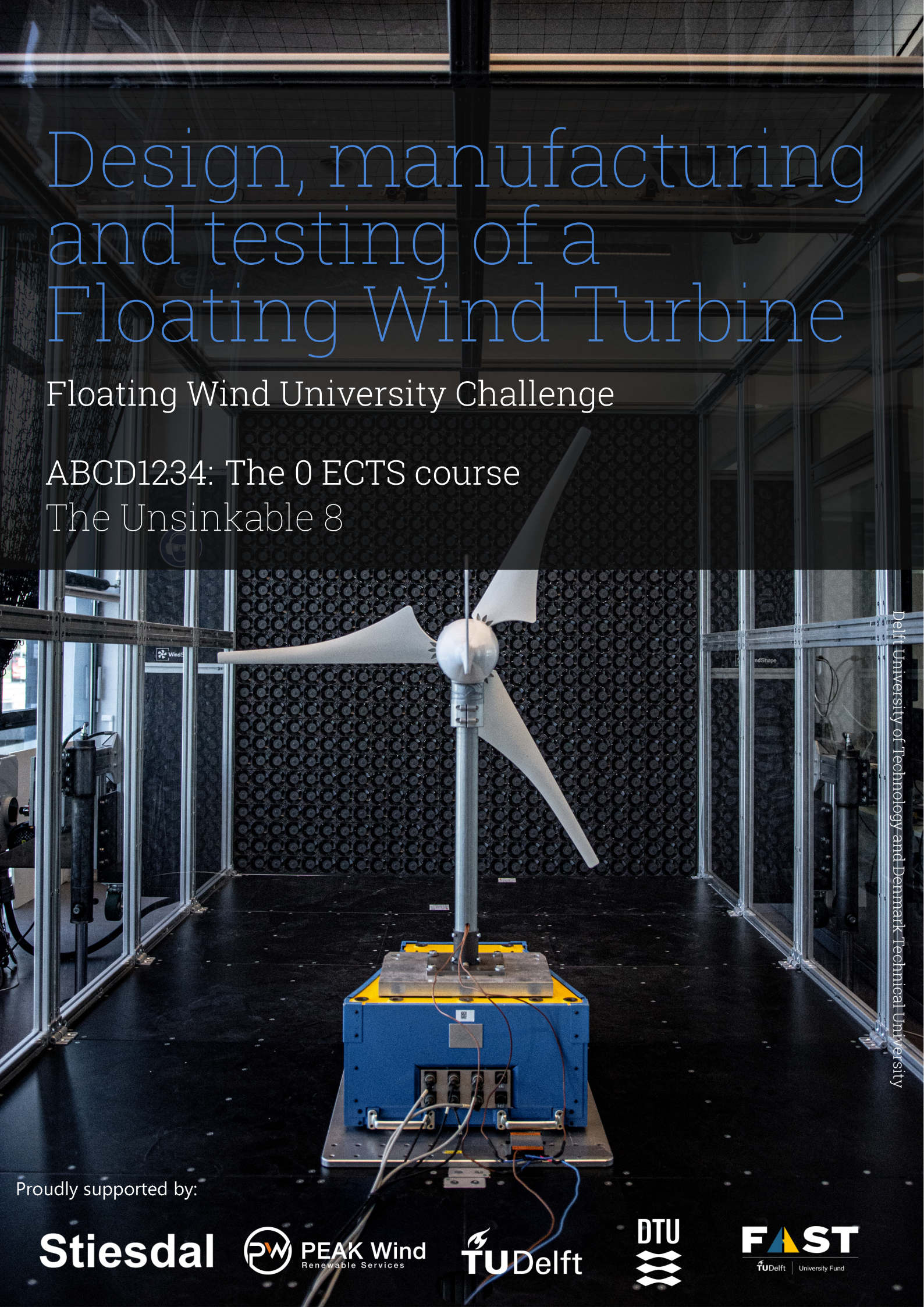

Delft University of Technology and Denmark Technical University

Proudly supported by:

Stiesdal

PEAK Wind Renewable Services

TU Delft

DTU

FAST TU Delft University Fund

Design, manufacturing and testing of a Floating Wind Turbine

Floating Wind University Challenge

by

The Unsinkable 8

Student Name	Student Affiliation
Karystinou, Dimitra	Sustainable Energy Technology, MSc, TU Delft
Scarlatti, Luca	Sustainable Energy Technology, MSc, TU Delft
van Putten, Sebastiaan A.G.	Wind Energy, MSc, Denmark Technical University
Forest, Joshua P.	Wind Energy, MSc, Denmark Technical University
Caruso, Mateo A.V.	European Wind Energy Master, MSc, TU Delft and Denmark Technical University
Folmar, Eric T.	European Wind Energy Master, MSc, TU Delft and Denmark Technical University
Iyer, Sowmya S.	European Wind Energy Master, MSc, TU Delft and Denmark Technical University
Perez Moreno, Carlos	European Wind Energy Master, MSc, TU Delft and Denmark Technical University

Project Duration: December, 2022 - May, 2023
Faculty: Faculty of Aerospace Engineering, TU Delft
Department of Wind Energy, DTU

Cover: AI Wind Tunnel Testing at 3me Faculty, TU Delft, picture by M. A. V. Caruso
Style: TU Delft Report Style, with modifications by Daan Zwaneveld and Carlos Perez Moreno

Acknowledgements

We would like to express our sincere gratitude to the companies and institutions that have supported us throughout this project.

We extend our deepest thanks to Stiesdal for their unwavering financial support, which has enabled us to carry out our research and development activities. We are also grateful for the valuable feedback and support they provided, which has helped us to refine our approach and achieve our goals. Additionally, we are grateful for the opportunity to visit their offices and network with their team, which has enriched our understanding of the industry and broadened our perspectives.

We would like to acknowledge the generous support of Peak Wind, whose financial contributions and technical expertise have been instrumental in the success of our project. We are particularly grateful for their marketing advice, which has helped us to reach a wider audience and raise awareness of our work. Their technical support has also been invaluable, enabling us to overcome challenges and make progress towards our goals.

Our thanks also go to Delft University Wind (DU Wind), who provided us with financial support and supervision. We would like to extend our appreciation to two of their professors, who lent us their expertise and guidance throughout our project. Their support has been instrumental in enabling us to develop our ideas and refine our approach.

We would also like to thank Antonio Pegalajar-Jurado and Fabio Pierella at the Technical University of Denmark (DTU Wind Energy Systems) who contributed valuable insight into floating substructures throughout the project.

We are grateful to the supervisor of the AI Wind Tunnel, who generously allowed us to use the wind tunnel for our turbine tests. This has been a critical component of our research, and we are grateful for the opportunity to conduct our experiments in such a cutting-edge facility.

Finally, we would like to thank Offshore Wind 4 Kids for organizing the challenge and providing monetary support, as well as the wind turbine generator. Their contributions have been essential in enabling us to carry out our research and achieve our goals.

The Unsinkable 8
Delft, April 2023

Contents

Preface **i**

1 Introduction **1**
1.1 Importance of floating offshore wind energy . . . 1
1.2 Project overview . . . 1

2 Wind Turbine Generator and Tower Design **3**
2.1 Wind Turbine . . . 3
2.1.1 Wind tunnel tests . . . 3
2.2 Tower Design . . . 7

3 Hydrodynamic design and analysis **8**
3.1 Floating platform geometry . . . 8
3.1.1 Hydrostatic stiffness matrix . . . 10
3.1.2 Pitch stability . . . 12
3.2 CAD and mesh generation with Salome . . . 13
3.3 Hydrodynamic analysis with NEMOH . . . 14
3.3.1 Mesh sensitivity analysis . . . 15
3.3.2 Validation with OrcaWave . . . 15

4 Mooring lines and anchors **17**
4.1 Choosing the system type . . . 17
4.2 Catenary mooring system geometric constraints . . . 18
4.3 Catenary system stiffness analysis . . . 19
4.4 Anchor selection . . . 21

5 Reduced order model and simulations **22**
5.1 Equations of motion . . . 22
5.1.1 Mass matrix . . . 22
5.2 Decay tests and natural frequency identification . . . 22
5.3 Response to wind and waves . . . 23

6 Manufacturing process **29**
6.1 Floating platform elements . . . 29
6.2 Mooring Lines and Anchors . . . 30

7 Concept scalability and financial analysis **32**
7.1 Criteria for scaled design . . . 32
7.2 Manufacturing and Materials . . . 33
7.3 Structural considerations . . . 33
7.4 Mooring considerations . . . 33
7.5 Operations and maintenance considerations . . . 34
7.6 Energy and Export Infrastructure . . . 34
7.7 Expected Construction and Operating Costs . . . 34

8 Conclusion **36**

A Mooring stiffness terms **37**
A.0.1 Single mooring line stiffness matrix, without transformations . . . 37
A.0.2 Full mooring matrix terms, for a single mooring line . . . 37

1 Introduction

1.1. Importance of floating offshore wind energy

In recent years, the renewable energy sector has seen a rapid increase in the development of offshore wind energy. As conventional bottom-fixed offshore wind turbines face limitations in terms of depth and seabed conditions, floating wind turbines have emerged as a promising alternative that can harness the stronger and more consistent wind resources found in deeper waters. Floating wind turbines can also be deployed further offshore, reducing visual impact and increasing public acceptance. Additionally, the wind resource is better further offshore, leading to a larger AEP of the wind farm.

This project report details the design, manufacturing, and testing of a floating wind turbine. In addition to presenting our team's efforts in developing a cost-effective and reliable floating wind turbine, this report aims to provide an overview of the latest developments in floating wind energy and emphasize the importance of small-scale testing for optimizing design concepts.

Recent developments in floating wind energy have shown that the technology is rapidly advancing, with more projects being proposed and commissioned globally. According to the latest data from the International Energy Agency, the global installed capacity of floating wind turbines is expected to increase significantly, with Europe leading the way in terms of installed capacity. This represents a significant opportunity for renewable energy generation, but also highlights the need to find new and optimized concepts that can increase energy efficiency and reduce costs.

In this context, small-scale testing plays a crucial role in identifying and refining new concepts that can be scaled up for commercial deployment. By testing and validating different design concepts under controlled conditions, researchers can identify the most promising solutions that can be further developed and optimized. Therefore, the Floating Wind Challenge focus on small-scale testing to evaluate the performance of floating wind turbine concepts can potentially allow to identify areas for improvement.

Overall, this project report contributes to the ongoing efforts to develop and deploy reliable and cost-effective floating wind turbines. We hope that our insights and findings will inform future research and development efforts, ultimately accelerating the deployment of floating wind energy and reducing dependence on fossil fuels.

1.2. Project overview

The design of the full system is based on a series of inputs, namely, the wind turbine generator provided by the competition organizers, and the met-ocean conditions at the challenge location. Furthermore, an iterative design process must be followed to refine the design, for which the main steps are shown in Figure 1.1.

Firstly, the wind turbine, a Vevor 400W model[1], is analysed, considering aspects such as mass, rotor diameter, and other overall dimensions. Together with the product description, a power curve

[1] See more information and product description in https://eur.vevor.com/wind-turbine-c_10731/12v-3-fiber-blades-horizontal-axis-small-sized-wind-turbine-generator-400w-p_010173302005?gclid=Cj0KCQjwuuKXBhCRARIsAC-gM0hBb6jvYwRVN1VD4iyVcge3t2r5CXsJHVByqnQVacbCb0QygUfhNH4aAiC0EALw_wcB

is provided. Information regarding the aerodynamic forces, that is, the thrust and torque, needs to be obtained by means of wind tunnel testing. The procedure and results are described in chapter 2. Additionally, the geometry of the WTG poses a hard constraint on the tower design, explored further in chapter 2.

Given the challenge location, the water depth range and met-ocean conditions, as well as the wind turbine - tower system design, the floating platform must be sized and optimized for static and dynamic performance. A thorough hydrostatic analysis is performed, followed by the hydrodynamic properties' calculation. This is shown in chapter 3.

The mooring lines and anchors affect greatly the stability in several aspects, for that reason several iterations are performed while sizing the floating platform. The process is described in chapter 4.

Finally, to integrate the wind turbine generator, tower, floating platform, mooring and anchors, a reduced-order model is developed and implemented, in order to analyze the dynamic response of the floater under different met-ocean conditions. The model and simulation results are shown in chapter 5.

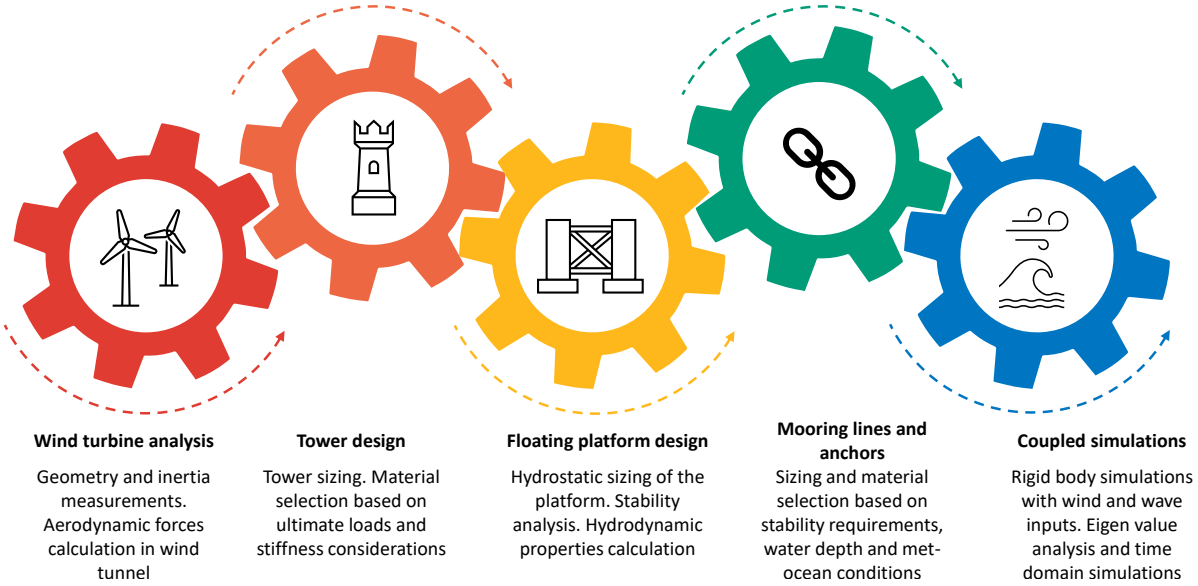

Figure 1.1: General floating offshore wind turbine design workflow

The aforementioned steps lead to a prototype design, suited for the location. In chapter 6, the manufacturing approach is described. It is important to notice that several manufacturing constraints have been included in the system design, such as material availability, geometrical constraints, techniques that could be applied in the construction, etc.

Finally, coinciding with the project objective of supporting the roll out of industrial scale of commercially viable floating platforms, a preliminary sizing of the floater, as well as a financial analysis of the design is provided in chapter 7.

The conclusions of the project are briefly outlined in chapter 8, together with the limitations of the approach used and further studies suggested for the continuation of the student project as part of the floating wind technology learning process.

2

Wind Turbine Generator and Tower Design

This chapter will present the characteristics of the wind turbine generator and of its tower. Several wind turbine characteristics, such as its thrust were not readily available to the team and were determined experimentally as will be covered in section 2.1. The design choice for the tower is discussed in section 2.2.

2.1. Wind Turbine

The main properties of the Wind Turbine Generator (WTG) are shown in Table 2.1. The WTG can be seen in Figure 2.4, where the turbine stands on top of its tower, and connected to a load balance, inside the Wind AI Lab at TU Delft.

Table 2.1: WTG Vevor 400W Main parameters

Parameter	Symbol	Value
Mass	m_{RNA}	5.86 kg
Rotor diameter	D_r	1.21 m
Torque control	-	Maximum Power Point Tracking (MPPT)
Above-rated operation control	-	Stall regulation
Nacelle length	L_{ncl}	0.67 m
Nacelle height	H_{ncl}	0.15 m
Nacelle width	-	0.15 m

2.1.1. Wind tunnel tests

The main objectives of the wind tunnel tests are to determine the turbine's thrust curve and use it as the aerodynamic force for the simulations. The power curve was also measured, to try and determine the optimal operating range for maximum power generation. Additionally, it is expected that the generator torque will impact the roll motion of the floating platform and other degrees of freedom when the rotor yaws.

Initially, the idea was to create a Blade Element Momentum Theory (BEM) code with an integrated dynamic inflow and dynamic stall model, that could be coupled with the hydrostatic and hydrodynamic forcing at the base of the tower, to use as an initial estimate for the decay periods and excitation frequencies. However, since the blade polar data was unavailable, an initial idea to make a mould of the blade and then draw the blade sections was implemented. Ten blade sections from the tip to the root at every 5 cm were drawn and digitised into points, and put into X-foil to obtain the polar data. Figure 2.1 shows the blade element outlines used to obtain the polars. However, this method came with a substantial errors in the measurement and the data and hence, it was not used and a wind tunnel test was conducted instead.

The wind tunnel test was conducted at the Wind AI Lab at TU Delft. The tunnel is a 2m x 2m test section with a series of small fans. A 3-axis force balance was used to measure the forces in the three directions as well as the respective moments. Figure 2.2 shows the maximum loading in each direction the balance can record, and Figure 2.3 showing a diagram of the load balance. Since the maximum moment would be due to the thrust, and the second largest due to the rotor torque, the balance was reoriented such that the y-direction faces the wind. This way, the moment due to the thrust would be in the X-direction, which takes the maximum load, and the moment due to the torque would be in the Y-direction with the second largest allowed load. The rotational speed of the turbine was measured using a hand-help tachometer and the power was calculated as the torque multiplied by the rotational speed. It was verified against the power calculated from the load box connected to the wind turbine generator. The moment due to the tower torsion was negligible.

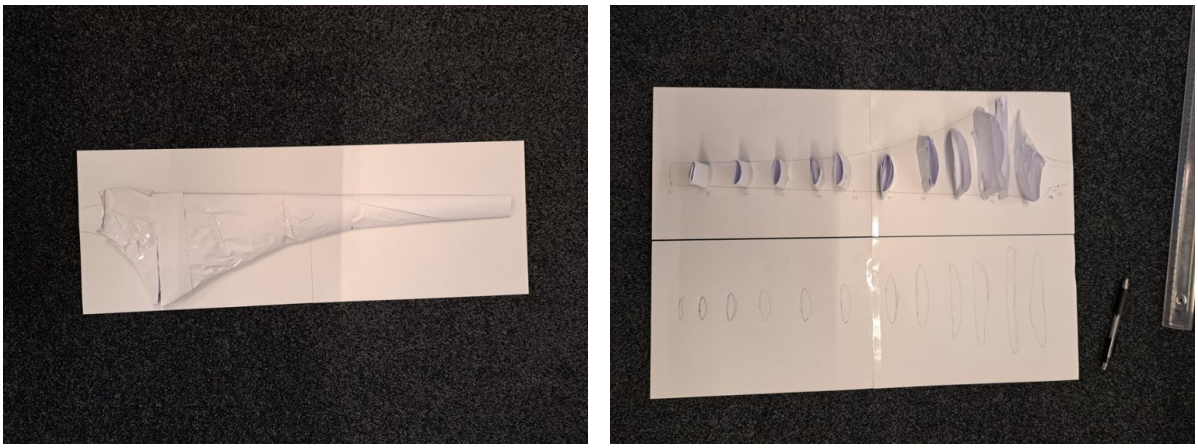

(a) Blade Model **(b)** Airfoil Sections

Figure 2.1: X-foil Blade Polar Method

Component			**Component**	
Axial Force	$F_x = \pm 250$ N		Rolling Moment	$M_x = \pm 500$ Nm
Side Force	$F_y = \pm 500$ N		Pitching Moment	$M_y = \pm 250$ Nm
Vertical Force	$F_z = \pm 500$ N		Yawing Moment	$M_z = \pm 50$ Nm

Figure 2.2: Maximum Loading for the Balance

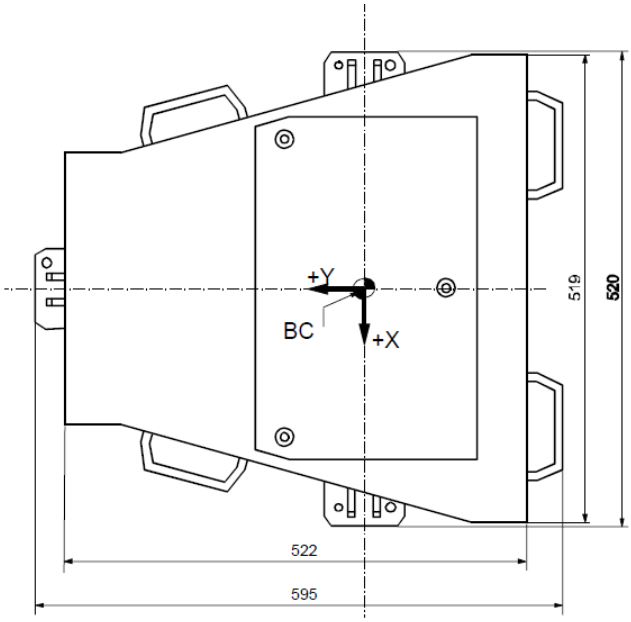

Figure 2.3: Top view of the load balance used during the wind tunnel testing.

Figure 2.4 shows the turbine mounted onto the force balance in the wind tunnel.

Figure 2.4: Test Section

The forces and moment in each axis were measured and used to calculate the thrust and power. The thrust curve is seen in Figure 2.5

A second order polynomial was fit to the curve of the thrust against the wind speed and used as the input for the simulations.

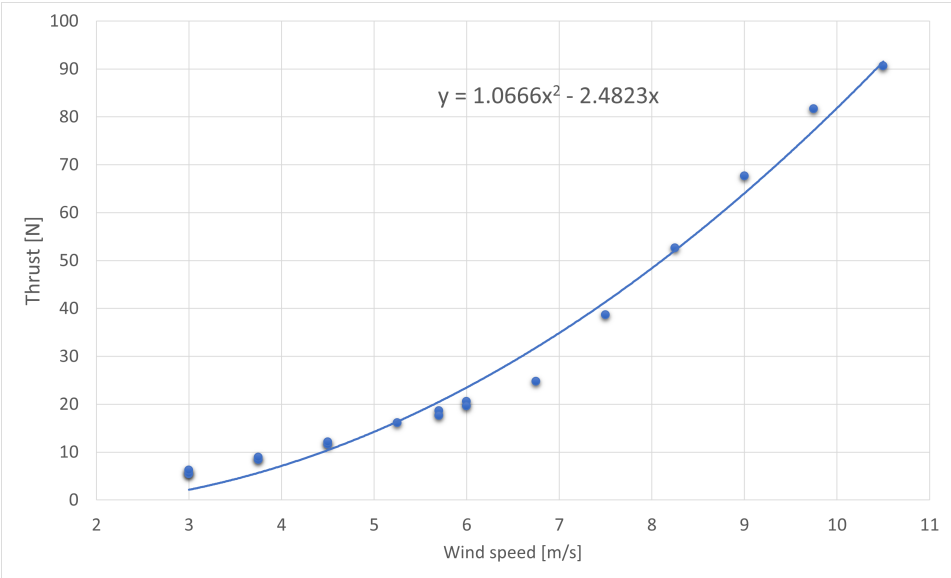

Figure 2.5: Measured thrust curve in the experiment performed at the Wind AI Tunnel

2.2. Tower Design

The tower design is largely a result of the materials that were readily available when setting up the wind tunnel test. A steel tube section of sufficient length was available that fit well into the bottom of the rotor-nacelle assembly, so it was used for the tests. The chosen tube is sufficiently thick to exceed any structural requirements such as compressive and bucking strengths. Following successful wind tunnel testing, it was decided that the same tube could be used as the final tower and elsewhere in the floater assembly (see chapter 6), since there was more of it available to be cut to the sizes required. Besides, it was relevant to assume a rigid tower to reduce the introduction of discrepancy in modelling the floater. As such, choosing steel for the tower allows for a stiff connection between the turbine and the floater. The main tower parameters can be seen in Table 2.2

Table 2.2: Tower main parameters

Parameter	Symbol	Value
Height	H_t	1.5 m
Outer diameter	$D_{t,o}$	0.05 m
Inner diameter	$D_{t,t}$	0.0475 m
Thickness	t_t	0.00125 m
Material (density)	ρ_t	Steel (8000 kg/m^3)
Total mass	m_t	10 kg

3

Hydrodynamic design and analysis

The hydrodynamic design is done using a series of open-source tools, such as Salome and NEMOH, with the aim of allowing future students and/or researchers to reproduce the workflow easily without needing often expensive licenses. The main purpose of the hydrodynamic analysis is to obtain the primary hydrodynamic properties and forces, which are then input in the reduced-order model, presented in chapter 5.

3.1. Floating platform geometry

The hydrostatic analysis of the floating platform is based on the wind turbine generator and tower constraints and its own geometry. The initial design is a three-cylinder triangular structure, as shown in Figure 3.1. Furthermore, cylindrical heave plates are considered at the bottom of the cylinders.

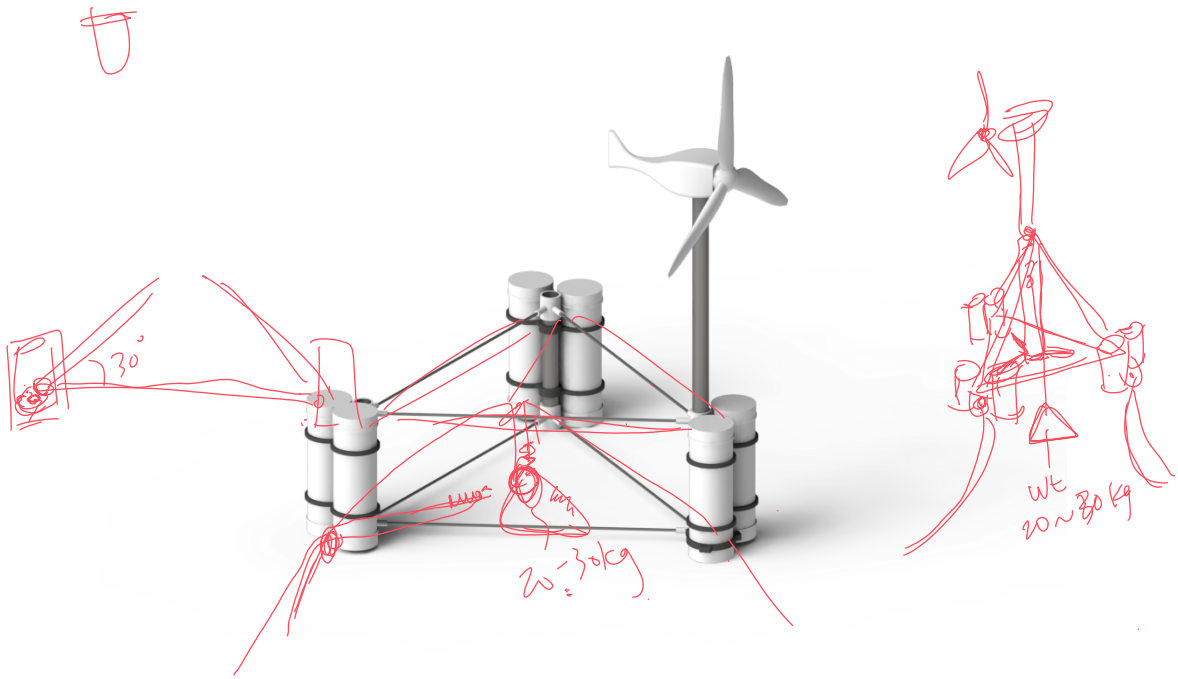

Figure 3.1: Floater concept render, without heave plates included in the visualization

A plan view can be seen in Figure 3.2. A double-buoy-per-vertex configuration is considered, due to limitations on the diameter of the cylindrical buoys (see Table 6.1). Furthermore, the modular design

allows for more or less buoyant elements to be added, changing the dynamic performance of the floater. This enables rapid validation of simulation data, and the ability to fine-tune buoyency and ballast.

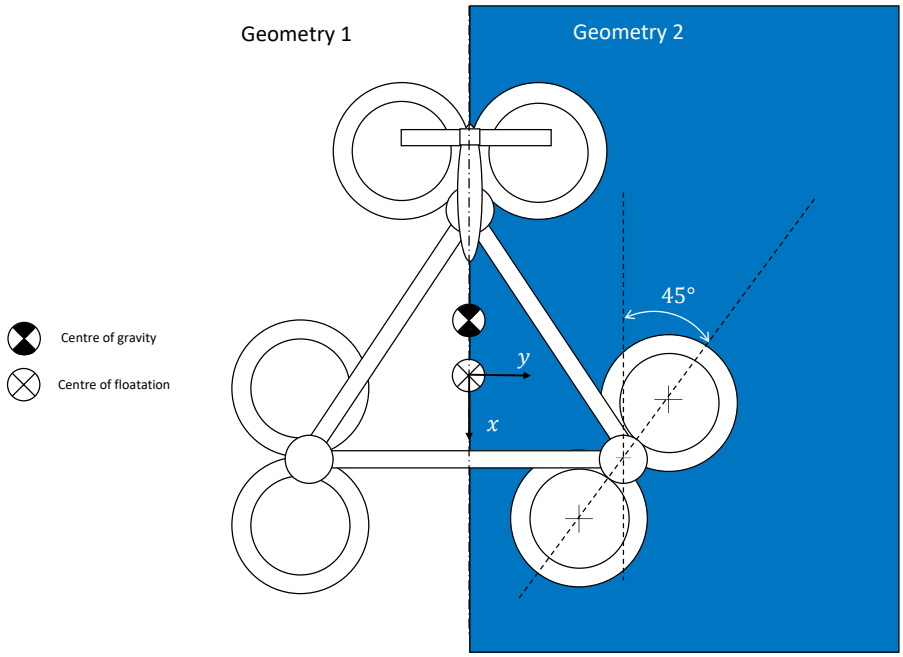

Figure 3.2: Floating platform plan view of the geometry

The first step in the calculation of the hydro-static properties is the calculation of the draft, by means of imposing a balance of the buoyancy force with the gravitational forces, as shown in [1]. For simplicity, geometry 1 is analyzed.

The total buoyancy of the floater is given by

$$F_{\nabla} = \rho_w g \nabla_{floater} \tag{3.1}$$

where $\rho_w = 1025$ kg/m^3 is the water density, $g = 9.81$ m/s^2 is the acceleration due to gravity, and $\nabla_{floater}$ is the volume of water displaced by the submerged part of the floater,

$$\nabla_{floater} = \nabla_b + \nabla_{hp} + \nabla_{fe} + \nabla_{se} \tag{3.2}$$

where, the volume of the buoys, heave plates, frame elements and secondary elements have been considered. They are calculated as follows,

$$\nabla_b = \pi \left(\frac{D_b}{2}\right)^2 H_b, \qquad \nabla_{hp} = \frac{\pi}{4} D_{hp}^2 t_{hp}, \tag{3.3}$$

$$\nabla_{fr} = \pi \left(\frac{D_{fr}}{2}\right)^2 L_{fr}, \qquad \nabla_{hs} = \pi \left(\frac{D_{hs}}{2}\right)^2 H_{hs} - \pi \left(\frac{D_{hs}}{2} - t_{hs}\right)^2 H_{hs} \tag{3.4}$$

The main elements providing buoyancy are primarily the cylindrical buoys, and, in a reduced scale, the heave plates, frame elements and shafts, due to their relatively small thickness.

On the other hand, to calculate the weight of the structure, all elements are considered, and additionally, a ballast mass, m_{ba} added identically to all the buoys is defined, such that the draft of the floater can be adapted, thus, the mass of the whole system is given by

$$m_{FOWT} = m_{RNA} + m_t + m_b + m_{hp} + m_{fe} + m_{hs} + m_{se} + m_{ba} \tag{3.5}$$

Where the mass of each floater element is calculated as its volume times the density times the number of elements used. The calculations are performed for $n_b = 6$ (buoys), $n_{fe} = 6$ (frame elements), $n_{hp} = 6$ (heave plates), and $n_{hs} = 3$ (hollow shafts).

Applying the balance of buoyancy and weight, the draft T is given by

$$F_{\nabla} = F_g \longrightarrow T = \frac{m_{FOWT} - \rho_w \left(\nabla_{hp}\right)}{\rho_w \cdot \pi n_b \cdot D_b^2/4} \tag{3.6}$$

where the displaced volume by the frame elements have been neglected as a first approximation. The flotation condition is set such that the concept is floating if $T > H_b$. The main drivers of the draft are the mass used as ballast and the height of the buoys. A quick sensitivity analysis is performed in these parameters, using the reference values in Table 6.1. The linear effect expected from the equations can be seen in Figure 3.3.

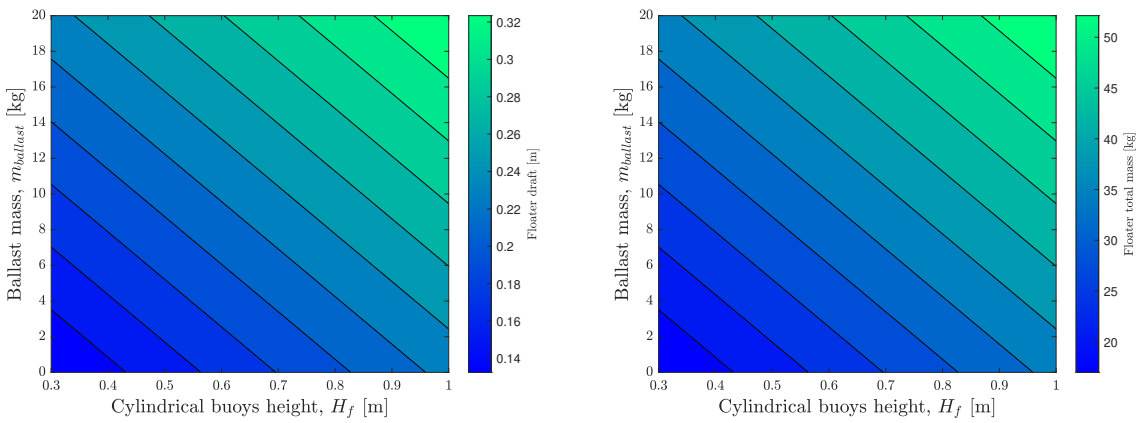

(a) Draft sensitivity

(b) Floater mass sensitivity

Figure 3.3: Sensitivity analysis in the draft and mass calculation to the ballast mass and to the cylindrical buoy height

3.1.1. Hydrostatic stiffness matrix

To further assess the stability of the floater as a function of the parameters previously defined we can use the hydrostatic stiffness matrix, which can be calculated relative to the flotation centre as

$$\boldsymbol{C_{hs}} = \begin{bmatrix} 0 & 0 & 0 & 0 & 0 & 0 \\ 0 & 0 & 0 & 0 & 0 & 0 \\ 0 & 0 & \rho_w g A_0 & \rho_w g I_2^A & -\rho_w g I_1^A & 0 \\ 0 & 0 & \rho_w g I_2^A & \rho_w g I_{22}^A + mg\left(z_b - z_g\right) & -\rho_w g I_{21}^A & -mg\left(x_b - x_g\right) \\ 0 & 0 & -\rho_w g I_1^A & -\rho_w g I_{21}^A & \rho_w g I_{11}^A + mg\left(z_b - z_g\right) & -mg\left(y_b - y_g\right) \\ 0 & 0 & 0 & 0 & 0 & 0 \end{bmatrix} \tag{3.7}$$

Where the flotation centre is defined as the geometrical centre of the water-plane area. Its position along the centre-line can be approximated assuming that the water-plane area is uniformly distributed in the three triangle vertices, and thus it is assumed to be in the geometric centre of the equilateral triangle formed by the frame. Therefore, its position is given as a function of the braces length, as shown in Figure 3.4.

Several parameters are involved. Firstly, the water-plane area, A_0, provides stiffness in the heave direction. It is calculated for our geometry as,

$$A_0 = 6 \cdot \pi \frac{D_b^2}{2} \tag{3.8}$$

where the buoys are assumed partly submerged, the area of the hollow shafts to be negligible, and the braces to be above or below the still water level (SWL).

The linear moments of area, I_1^A and I_2^A, are both zero due to the symmetry. The second moment of area in the surge direction, I_{11}^A, is given by the sum of all cylinders' moments of area, plus a contribution from the translation to the x-axis using the parallel-axis theorem,

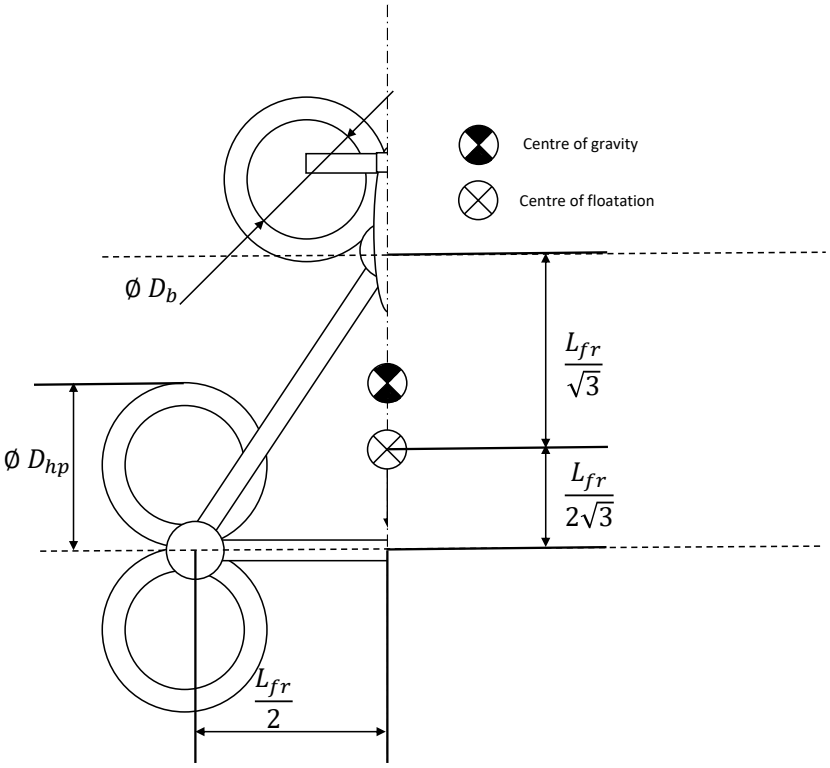

Figure 3.4: Main geometrical considerations for hydrostatic calculations

$$I_{11}^{A} = 6 \cdot \frac{\pi}{64} D_b^4 + \cdot \frac{\pi}{2} D_b^2 D_{hp}^2 + \frac{\pi}{4} D_b^2 L_{fr}^2 \tag{3.9}$$

The second moment of area in the

$$I_{22}^{A} = 6 \cdot \frac{\pi}{64} D_b^4 + 2\pi D_b^2 \left(\frac{L_{fr}^2}{3} + \frac{D_{hp}^2}{3} \right) \tag{3.10}$$

The product moment of area is given by

$$I_{12}^{A} = 2\pi D_b^2 \left(\frac{D_{hp}^2}{4} + \frac{L_{fr}^2}{12} + \frac{D_{hp} L_{fr}}{4} \right) \tag{3.11}$$

Next, the location of the center of gravity needs to be determined. A representation of the main elements involved in the calculation can be seen in Figure 3.5. In the vertical direction, z_{cg}, it is calculated by

$$z_{cg} = \frac{z_{cg_{rna}} m_{rna} + z_{cg,t} m_t + z_{cg,b} m_b + z_{cg,hp} m_{hp} + z_{cg,fr} m_{fr} + z_{cg,ballast} m_{ballast}}{m_{FOWT}} \tag{3.12}$$

The ballast is assumed to be concentrated at the bottom of the cylinders, and the braces mass it is assumed concentrated at the mid-height of the submerged part of the cylindrical buoys.

Similarly, the centre of gravity location in the surge direction is obtained as shown in Figure 3.6, neglecting the effect of the frame elements, as they are considered to be symmetrically distributed at both sides of the centre of gravity.

The location of the centre of buoyancy is obtained as the centre of the submerged volumes. In the z-direction,

$$z_{cb} = \frac{-\left(T - t_{hp}/2\right) \nabla_{hp} - \left(T - t_{hp}\right) / 2 \nabla_b}{\nabla_{FOWT}} \tag{3.13}$$

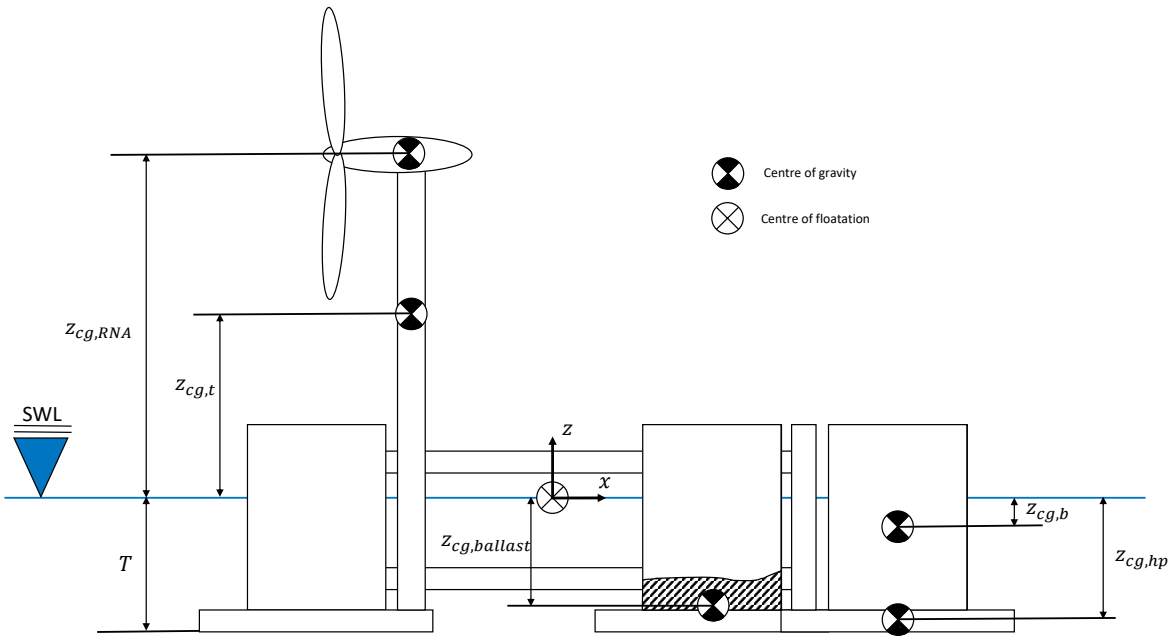

Figure 3.5: Side view floater main geometry with indications of the centre of gravity location for each element with respect to the SWL

Similarly, in the x-direction, assuming the volume is concentrated at the vertices, and the effect of the frame elements is neglected,

$$x_{cb} = \frac{-2\frac{L_{fr}}{\sqrt{(3)}}\left(\nabla_{hp} + \nabla_b\right) + 4\frac{L_{fr}}{2\sqrt{(3)}}\left(\nabla_{hp} + \nabla_b\right)}{\nabla_{FOWT}} \tag{3.14}$$

The location in the y-direction for both centre of gravity and centre of buoyancy is assumed zero, as there is symmetry in the design. However, a sensitivity analysis to misalignment of the elements should be conducted to determine the effect manufacturing imperfections can have in the stability of the floater in roll and yaw motions.

3.1.2. Pitch stability

The pitch-pitch stiffness, K_{55}, is often used as a measure of the hydrostatic stability of a floating platform. There are three main contributions,

$$K_{55} = \underbrace{\rho g I_{yy}}_{\text{waterplane area}} + \underbrace{\rho g \nabla z_B - m_{tot} g z_G}_{\text{B-G relative position}} + \underbrace{K_{\text{moor},55}}_{\text{mooring}} \tag{3.15}$$

For a semi-submersible floater, the main effect comes from the water-plane area, with smaller contributions from the relative position between the centre of buoyancy and the centre of gravity (also present in the hydrostatic stiffness matrix) and the mooring line stiffness in pitch. The two first terms on the right-hand side correspond to the hydrostatic contribution $C_{hs}(5,5)$, as can be seen in Equation 3.7.

Considering only the static behaviour of the floating wind platform, we can assume a moment acting on the y axis, τ_5, which would originate a pitch value θ_s, such that

$$K_{55}\theta_s = \tau_5 \tag{3.16}$$

If the moment originates from the thrust force, then $\tau_5 = F_a \cdot z_{cg,RNA}$, where F_a is the thrust force. Therefore, the thrust force that causes a pre-defined static pitch angle displacement is obtained simply as

$$F_{a,\theta} = \frac{K_{55}\theta_s}{z_{cg,RNA}} \tag{3.17}$$

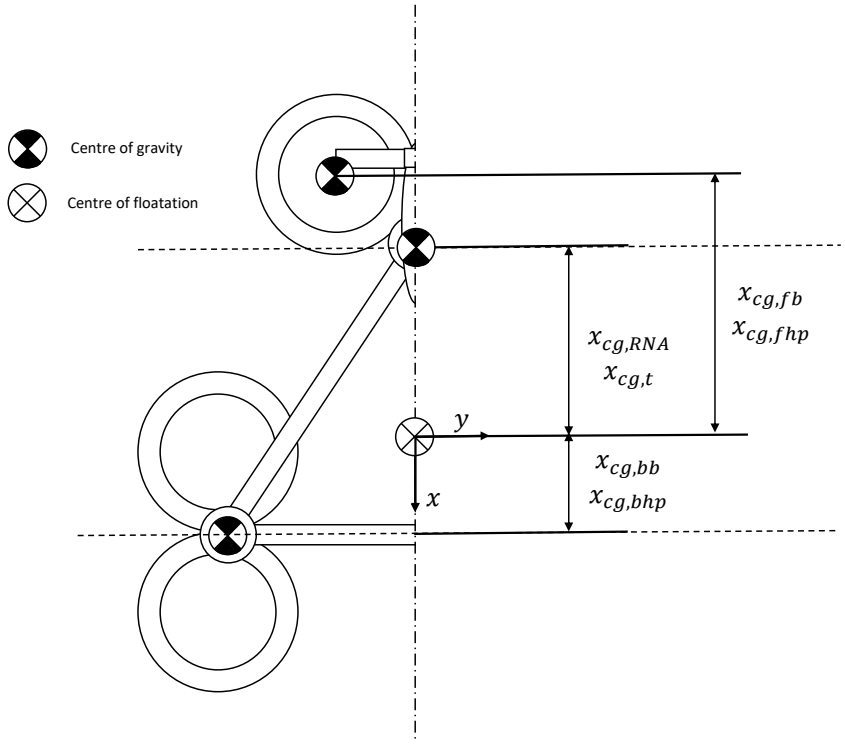

Figure 3.6: Plan view floater main geometry with indications of the centre of gravity location for each element with respect to the flotation centre

In Figure 3.7, the effect of the tower height and the length of the braces in $F_{a,\theta}$ is analyzed, for a fixed geometry and mooring stiffness. From the results, the significant coupling between both parameters and the pitch stiffness is obvious. Increasing the hub height dramatically causes the maximum allowable force to decrease, as the moment arm gets larger. On the other hand, a large increase of the allowable thrust is attained by using longer braces for the frame, as the second moment of area, I_{11}^{A}, the area becomes significantly larger. The effect of the frame size however requires careful considerations, as there are hydrodynamic effects involved, which will be treated in the following sections, as well as transportation and installation limitations that must be considered both for the small scale as well as for a commercial-size platform, as discussed in chapter 7.

Comparing the allowable thrust force to limit the platform pitch static displacement to the values obtained in the wind tunnel testing (see Figure 2.5), a design envelope can be traced, which limits the hub height to 1.5 m, and, aiming to maximize it, the braces length should be ≥ 1.6 m.

3.2. CAD and mesh generation with Salome

A simplified CAD model was generated using Salome, which is open-source software used for numerical simulations and modelling of complex geometries [2]. Salome was used for the development of the meshes of underwater geometry, which were afterwards entered into NEMOH to determine the floater's hydrodynamics.

The first step included the creation of the CAD model. Since this model aims to get some preliminary results on the hydrodynamic behaviour of the floater, a simplified model was used, including only the buoys and their respective heave plates, excluding the braces connecting the buoys and minor details of the manufacturing model. The CAD was created through a parameterized model with considering the primary properties of the geometry such as the diameter of the buoys and the heave plates, the height of the floater, the distance of the buoys apart and the draft that was derived from the hydrostatics and implies which part of the geometry will be meshed.

The following step included mesh generation. Salome offers the ability to develop different kinds of meshes, which is a property that was investigated along with simulation results. Triangular mesh is the most commonly used however for hydrodynamic applications and potential flow solvers like NEMOH,

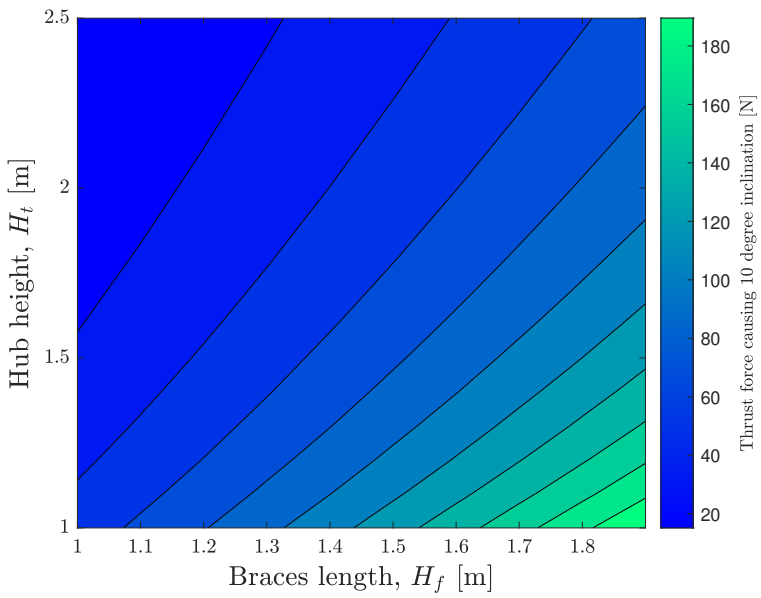

Figure 3.7: Sensitivity of the maximum thrust allowable to limit the static pitch displacement of the floating platform below 10 degrees, with respect to tower height and braces (frame elements) length

quadrangular meshes are most appropriate. To avoid uncertainty and use the optimum amount of elements, radial meshes were used like those in Figure 3.8a.

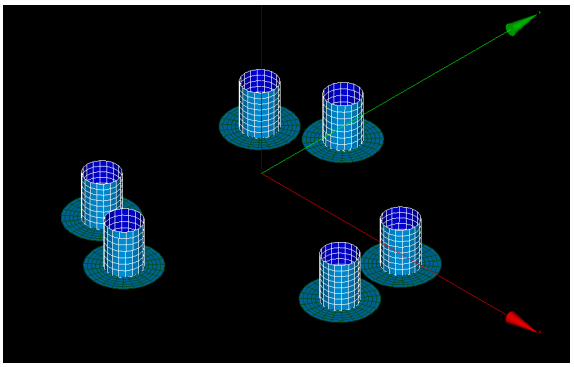

(a) Quadrangular mesh generated with Salome for double-buoys geometry

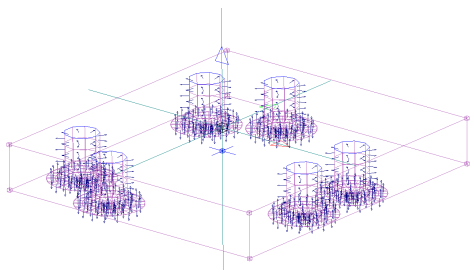

(b) Quadrangular mesh overview with BEM rosseta

3.3. Hydrodynamic analysis with NEMOH

The hydrodynamic analysis is performed using NEMOH [3], an open-source boundary element method solver developed by LHEEA Nantes. The software structure is shown in Figure 3.9. The purpose of NEMOH is to calculate the hydrodynamic behaviour of the floater itself by solving the radiation/diffraction problem over the floater-defined mesh. The generated mesh obtained from Salome is checked with BEM Rosetta and then converted to the form recognized by NEMOH. The main output that was studied was the RAOs with an emphasis on the added mass and the damping coefficients which are used in the reduced total model simulations. To reduce the simulation duration, the primary simulation characteristics have to be chosen. As a result, all of the simulations are conducted at 50 distinct frequencies, all of which fall within the range of the anticipated waves (0–20 rad/sec) and only unidirectional waves were considered.

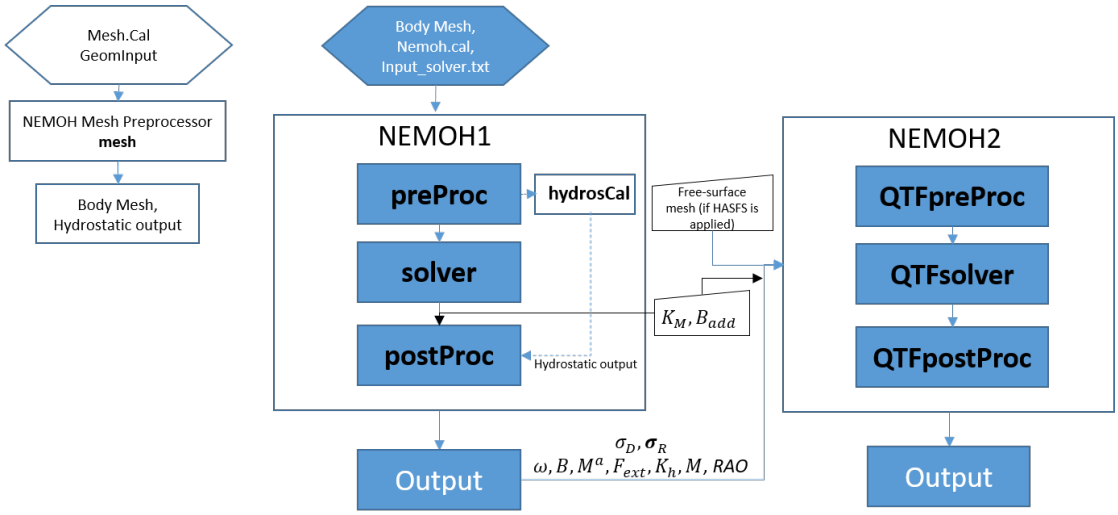

Figure 2: Global flowchart of NEMOH software

Figure 3.9: NEMOH Software workflow. Reprinted from [4]

3.3.1. Mesh sensitivity analysis

Apart from the decision over the mesh type, the number of elements had to be decided. Therefore, a sensitivity analysis over the different number of panels was conducted to give an implication about the optimum number of elements used. As shown in Figure 3.10 the results of damping and added mass coefficients over the surge, heave and pitch degrees of freedom are presented as shown, after 2000 panels the results are very close and tend to converge. As a result, all simulation run with around 2000 panels. It should be mentioned that before the finalization of the model, many mesh types and geometries were examined as part of the design iteration process, besides the number of meshes.

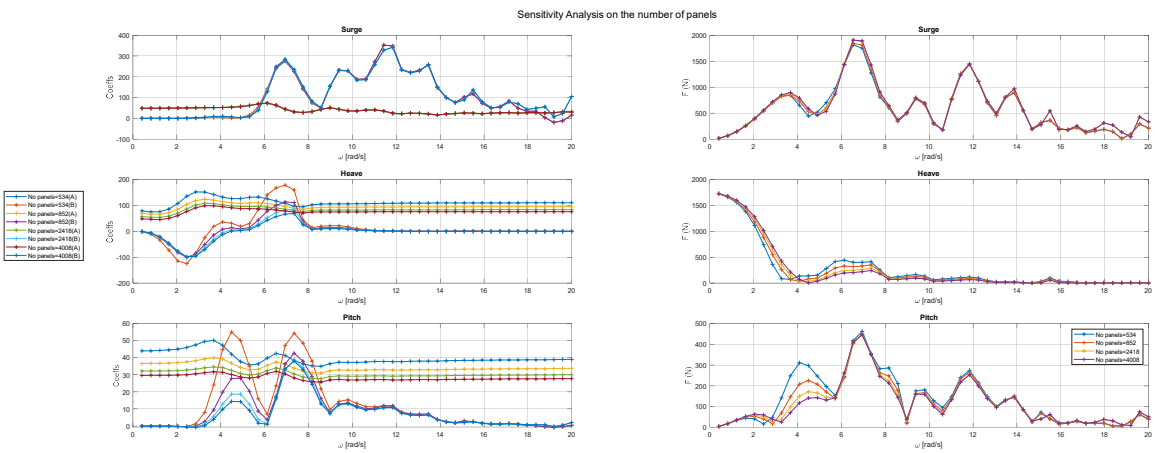

Figure 3.10: Sensitivity Analysis on the mesh fidelity

3.3.2. Validation with OrcaWave

The workflow followed with Nemoh has been partly validated with the commercial software OrcaWave. This diffraction code allows to easily perform diffraction/radiation calculations, and allowed to give an indication of possible improvements in the modelling and meshing processes with Salome. Some of

the results for a preliminary floater design can be seen in Figure 3.11. For most degrees of freedom there is a very good match in the results both in terms of the added mass and the radiation damping. However, for the case of heave, there is a significant mismatch in the added mass values, and also for long periods in the radiation. This may indicate a poor quality of the heave plates mesh[1].

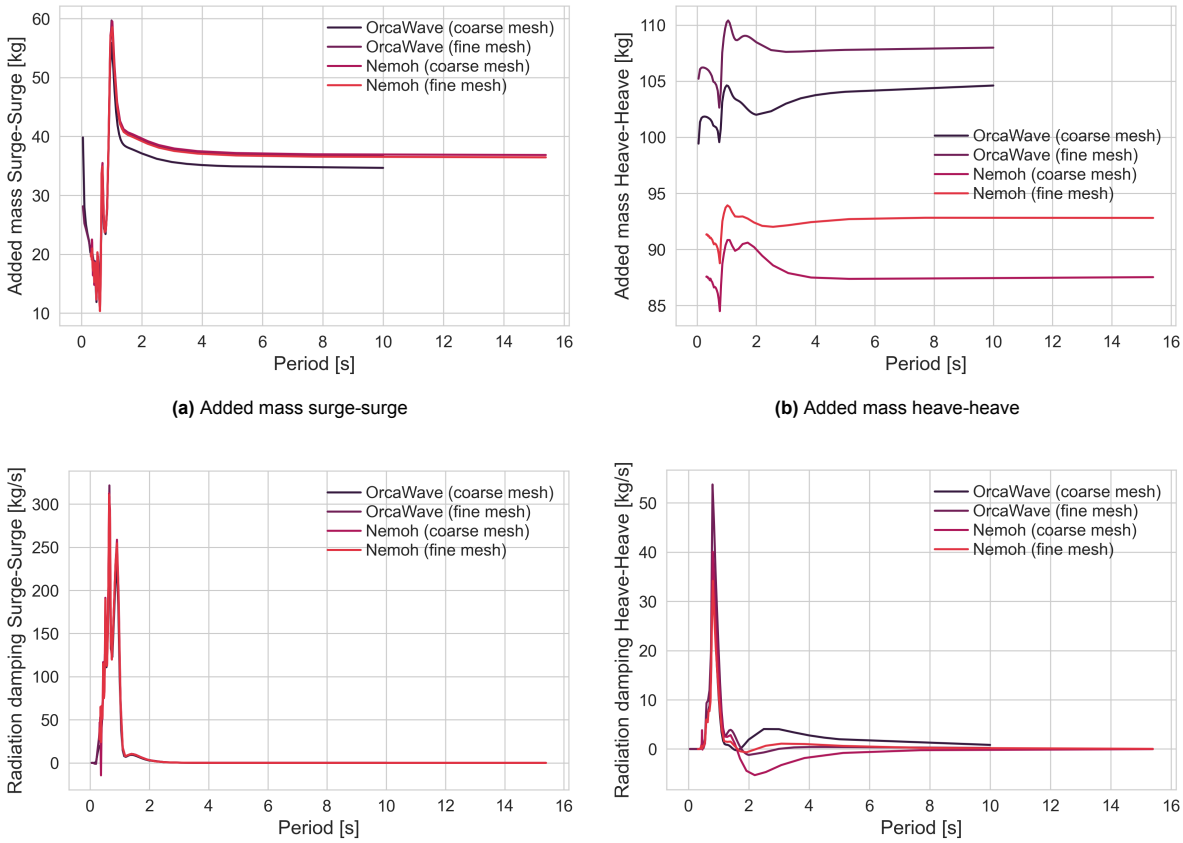

(a) Added mass surge-surge

(b) Added mass heave-heave

(c) Radiation damping surge-surge

(d) Radiation damping heave-heave

Figure 3.11: Validation of Nemoh results with OrcaWave radiation/diffraction code

[1]The mesh generation in the heave plates has been improved since the validation work was performed, and future comparisons may be presented at later stages of the project.

4

Mooring lines and anchors

The mooring and anchors system are critical for providing system stiffness in the water, particularly restoring stiffness in the surge, sway, and heave directions for a semi-submersible floater concept. The central part of the mooring concept is a pivot buoy fairlead connection, shown in Figure 4.1. The pivot buoy serves as a single point connection for the mooring lines, which allows for the floater to rotate with the current. Additionally, a single connection point reduces installation complexity.

4.1. Choosing the system type

The primary limitation considered during the preliminary mooring system design is the change in water depth expected during the installation and testing of the floater. Since the installation is in shallow water near the shore, both the wave heights and the change in tide dramatically change the proportional water depth. Specifically, at Scheveningen beach in the Netherlands where the floater concept will be installed, the tide is expected to reduce the mean water level by 0.5 meters during the installation and testing period, summarized in Table 4.1. Considering a peak wave height of 0.5 meters, the total expected range of water depths can vary by 1.5 meters. This is a significant amount considering that the installation water depth will be around 1.5 to 2 meters.

Three general mooring types were considered: taut mooring, tension-leg mooring, and catenary mooring. The advantages of taut mooring and tension-leg mooring are their relatively small footprints. However, the implementation of a tension-based mooring system which would need to maintain tension in both 2.15 m of water depth and 0.65 m of water depth without flooding the floater increases the complexity significantly. Either the floater would require a large splash zone, or the mooring lines would need to have an adjustable length, or a combination of both. The feasibility of manufacturing and operating a system with these requirements during the competition is quite low. Additionally, the requirements of the anchors in the seabed would be dramatically increased, and designing and installing anchors that would be sustaining large vertical loads in a seabed without a proper geotechnical survey would mean an unverifiable anchor system prior to testing. Installing vertical load anchors with limited access to necessary equipment for digging effectively also increases the challenges of such a system.

Therefore, a catenary mooring system was chosen, considering the limitations of water depth, anchors, and installation. With a catenary mooring system, the line length and anchor radius can be designed such that the lines will maintain a catenary shape for all water depths, further analysed in

Table 4.1: Mean, maximum, and minimum water depths expected from installation at 14:00 to the end of testing at 17:00 on May 12th, 2023 at Scheveningen Beach, Netherlands, assuming an initial installation mean water depth of 1.65 m and 0.5 m wave crests.

Time	Mean depth	Max depth	Min depth
14:00	1.85 m	2.35 m	1.35 m
15:30	1.50 m	2.00 m	1.00 m
17:00	1.35 m	1.85 m	0.85 m

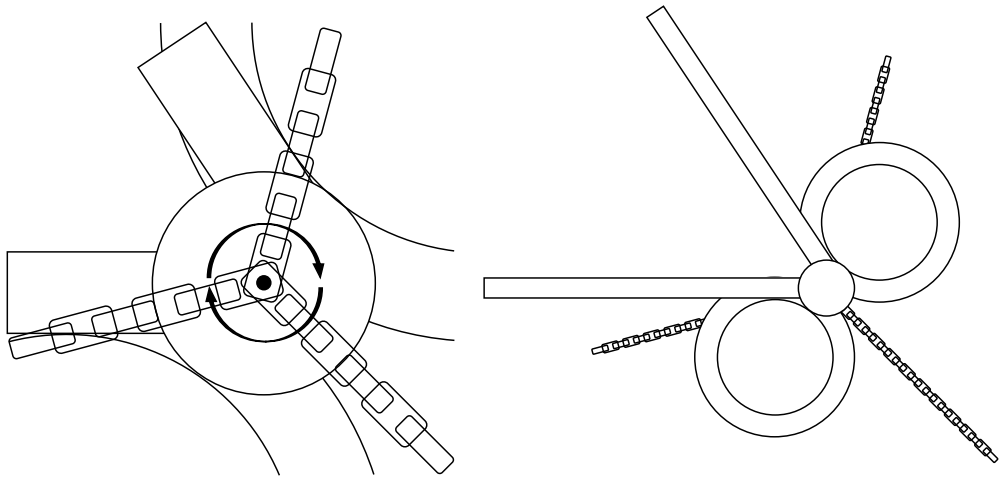

Figure 4.1: Illustration of the pivot buoy concept, showing both a view from below of the mooring connection with arrows showing the degrees of freedom allowed by the connection (left) and the above view (right) from a comparatively zoomed out perspective.

Figure 4.2. A catenary mooring line also has lower design requirements imposed on the anchors. With a catenary line with line resting on the seabed, the anchor needs only to be a horizontal load anchor, which is much easier for the team to design and install for the purposes of the competition. The remainder of this section focuses on the design and implementation of a catenary mooring system for the floating substructure.

4.2. Catenary mooring system geometric constraints

The catenary mooring system is constrained by several factors: the change in water depth, readily available materials, and the ease of installation of lines. First the water depth will be considered. The mooring line shape is geometry dependent, not weight dependent, and the mathematical definition is

$$l = L_0 - \frac{V}{w} + \frac{L_0 H}{EA} + \frac{H}{w} \text{arcsinh} \frac{V}{H} \tag{4.1}$$

$$h = \frac{1}{w}\left[\sqrt{H^2 + V^2} - H + \frac{V^2}{2EA}\right], \tag{4.2}$$

which cannot be calculated analytically. In the catenary mooring shape equation, l and h, H and V are the horizontal and vertical line distances and line tension components, respectively for single line constrained to a plane. L_0 is the line's original unstretched length, w is the line's weight per length in water, and EA is the line's material stiffness. For this analysis, the line is assumed to be infinitely stiff, $EA \to \infty$, so both the first term for calculating l and the fourth term for calculating h go to 0. Given the use of steel chain for the mooring system and the magnitude of expected tension forces experienced by the lines to be of order $10^2 to 10^3$ N, this is a fair assumption.

The mooring system is still particularly sensitive to water depth, which is demonstrated in Figure 4.2. This figure has been produced using limits derived from Equation 4.2. Given a range of possible fairlead connection heights from the seabed, h, then a minimum anchor radius can be determined which satisfies the constraints of being less than the tallest possible connection in the shallowest water depth and the shortest possible connection in the deepest water depth. The results show a particular sensitivity to shallow water rather than deep water.

The contour shows the minimum required anchor radius given the combination of deepest possible depth and shallowest possible depth along the left y-axis and x-axis, respectively. The installation is easier and the material costs are lower for the system if a smaller mooring footprint can be used, so the smallest possible anchor radius is desirable. However, the depth of the water for which the system can be installed safely and within the 90-minute time constraint by the team members during the competition

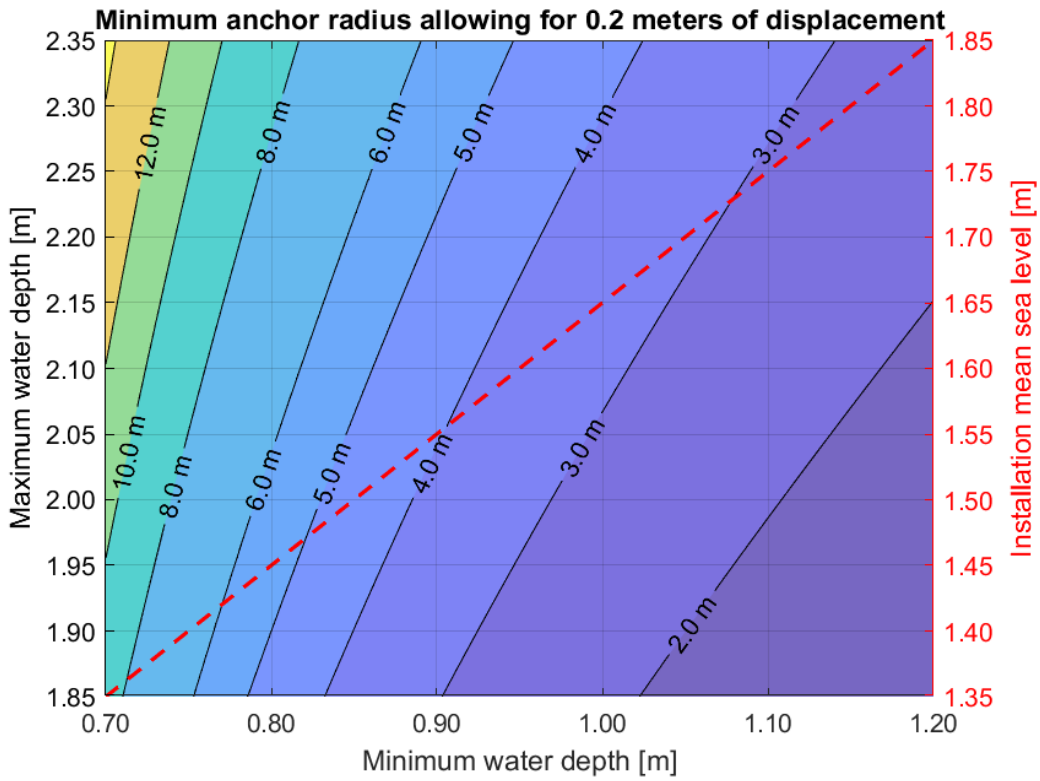

Figure 4.2: Mooring anchor radius contour plot, assuming a fairlead connection 0.27 m below SWL, a SWL decrease of 0.15 m, and $H_s = 1$ m. The red line follows the path along the contour with these values, and the design installation depth of 1.5 m has been chosen.

Table 4.2: Mooring system dependent geometry for representative and extreme water depths assuming static equilibrium for the mooring system. The system has unstretched line length $L_0 = 5.4$ m and anchor radius $l = 5.0$ m.

Description	Water depth	h	L_s
Minimum depth	0.85 m	0.58 m	0.69 m
Minimum MSL	1.35 m	1.08 m	2.06 m
Maximum MSL	1.50 m	1.23 m	2.64 m
Maximum depth	2.00 m	1.73 m	5.11 m

is another constraint to consider. A maximum installation mean sea level depth of 1.5 m at the time of the beginning of the testing period has been chosen (Table 4.1). Assuming a 0.2 m maximum allowable lateral displacement of the floater against a single line, a forecasted change in water depth of -0.15 m during the testing period, and 0.5 m extreme wave heights, the minimum allowable anchor radius is 4.5 m. To limit the required vertical loads for installation to 200 N between the three lines, this becomes a 5.0 m anchor radius with a 5.4 m mooring line, summarized in Table 4.2.

4.3. Catenary system stiffness analysis

The mooring system stiffness is formulated using an analytical approach of the change in the tension at the fairlead connection of floater from the lines from the system's position and orientation, from [5]. This gives the system's mooring static stiffness from a pre-calculated position for a displacement in each of the six degrees of freedom. The matrix formulation involves a lengthy derivation. The basic composition is shown in 4.3, with the terms in A.

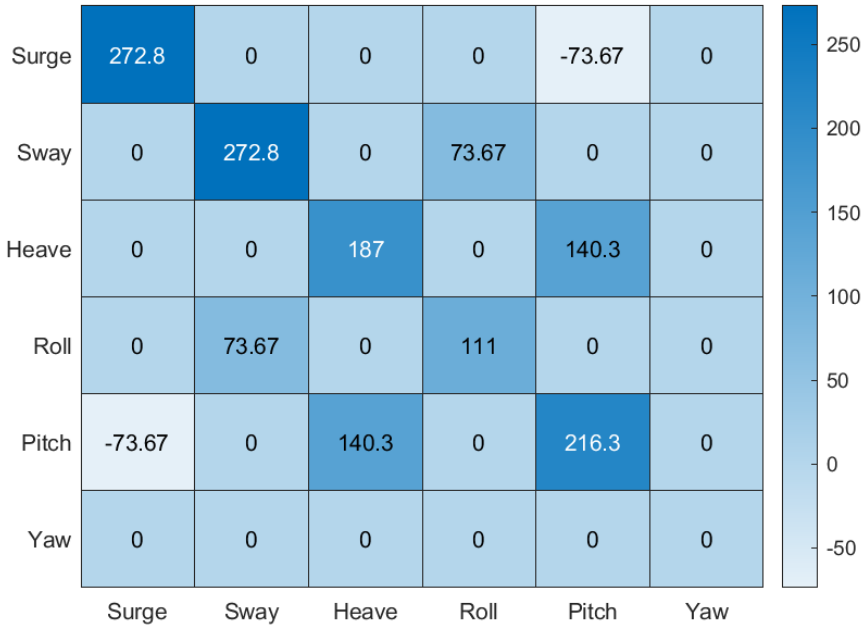

Figure 4.3: Mooring restoring stiffness contribution. The values have units N/m i,j = [1:3,1:3]; N/rad i,j = [1:3,4:6]; Nm/m i,j = [4:6,1:3]; and Nm/rad i,j = [4:6,4:6].

$$\mathbf{K}_{\text{moor}} = \begin{bmatrix} k_{11} & k_{12} & k_{13} & k_{14} & k_{15} & k_{16} \\ k_{21} & k_{22} & k_{23} & k_{24} & k_{25} & k_{26} \\ k_{31} & k_{32} & k_{33} & k_{34} & k_{35} & k_{36} \\ k_{41} & k_{42} & k_{43} & k_{44} & k_{45} & k_{46} \\ k_{51} & k_{52} & k_{53} & k_{54} & k_{55} & k_{56} \\ k_{61} & k_{62} & k_{63} & k_{64} & k_{65} & k_{66} \end{bmatrix} \tag{4.3}$$

The mooring system's primary responsibility is restoring stiffness to surge and sway motions in the floater. A representative water depth for a static sea state is 1.4 m of water depth with no lateral or rotational displacement. With the given mooring system, the stiffness contribution considering a 6 degree of freedom rigid body system is shown in Figure 4.3. The mooring system has symmetry for surge and sway, and their respective coupled terms with pitch and roll because of the single point connection. However, there is a stronger pitch stiffness than roll stiffness as well as pitch-heave coupling because the system's center of mass is off-center to the mooring connection point along the axis parallel to the primary direction of forcing. Additionally, it can be seen the strongest stiffness contribution is in the pitch and surge directions. There is no yaw stiffness contribution because of the assumed freely rotating pivot buoy connection.

Figure 4.4 shows the change in the surge/sway, heave, roll, pitch, and coupled surge/sway-pitch/roll stiffness terms with the change in water depth assuming static equilibrium. The system's stiffness changes with water depth, as more or less line is suspended of the whole length as the depth increases or decreases. The surge and sway stiffness and the coupled surge/sway-pitch/roll terms are especially and equally sensitive, increasing more than 3 times as much for increase in water depth to 2.0 m and decreasing to 0.2 times their respective values for 1.4 m. Roll is next most sensitive, followed by pitch, which again is related to the off-center-of-gravity attachment of the mooring on the pitch axis. Heave stiffness, however, has almost the same value for the full range of water depths. This can be explained by the fact that the amount of line being lifted off the seabed or being set onto the seabed is almost equal for a purely vertical motion for all water depths considered. The system however cannot be tightened more, since with the deepest water depth in static equilibrium 5.11 m of the 5.4 m line is lifted off the seabed, and the anchors should not be subjected to vertical loads.

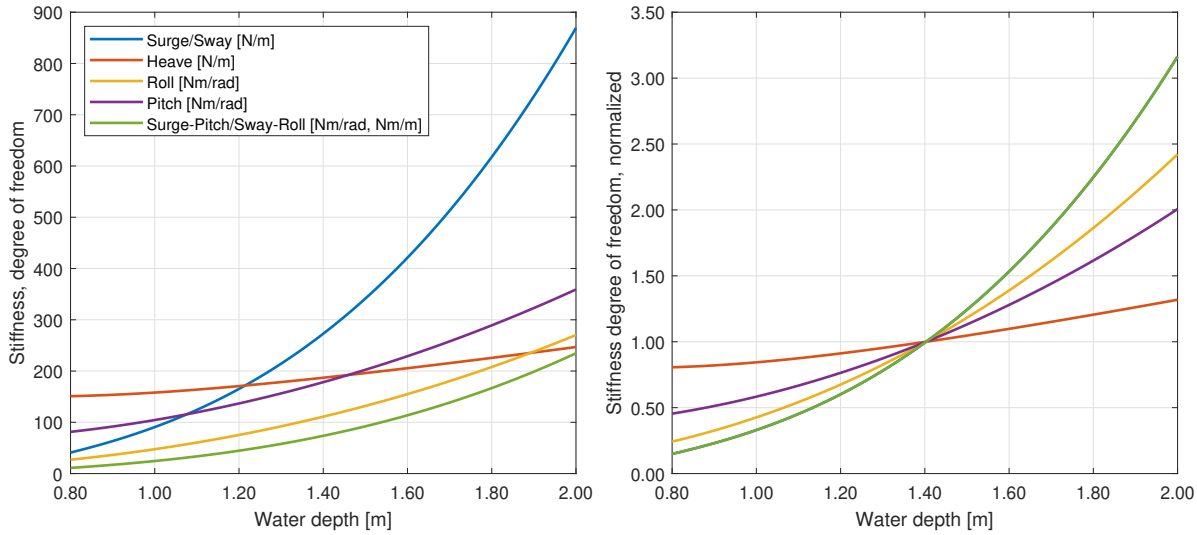

Figure 4.4: Mooring system stiffness contribution sensitivity to water depth, with units (left) and normalized to the 1.40 m water depth static equilibrium value (right).

4.4. Anchor selection

The anchor selection is driven by the mooring system design loads. There are several options possible for anchors. Limiting the choice to anchors easily installed by hand without extensive equipment results in an option between clump weight anchors and an anchor driven into the seabed. In the context of the competition, only extreme loads are considered. The maximum static loading in a single line is 140 N, and given the catenary lines will only be applied in a horizontal direction. Therefore, an anchor which is easily installed and can resist horizontal loads is desired. Clump weights are challenging to install in water by lifting and carrying, and could pose a danger to the teammates installing them. Therefore, a driven stake has been proposed for installation, which is both easier to carry to the location for installation and also to position more precisely. Again, there is a lack of geotechnical survey in the testing area, so the number of driven stakes required to resist the expected loading will be tested beforehand.

5

Reduced order model and simulations

5.1. Equations of motion

The eigen-frequencies and the dynamics of the system are computed assuming the floating platform behaves as a rigid body, with six degrees of freedom (DOFs), and the aerodynamic and wave forces are computed as external forces, whereas the radiation and diffraction effects are considered as part of the inertia and damping terms. Similarly, the effect of the mooring lines is assumed linear, and included in the stiffness term. These assumptions lead to the following equations of motion (EOM),

$$\left(M_s + A\left(\omega\right)\right)\ddot{x} + B\left(\omega\right)\dot{x} + \left(C_{hs} + C_{moor}\right)x = F_{waves} + F_{aero} \tag{5.1}$$

Several of these matrices have been presented earlier. The hydrostatic stiffness is shown in subsection 3.1.1, and it is calculated using a MATLAB code developed by the team. The mooring line stiffness matrix is shown in chapter 4

5.1.1. Mass matrix

The mass matrix can be calculated as,

$$\boldsymbol{M}_s = \begin{bmatrix} m & 0 & 0 & 0 & mz_g & -my_g \\ 0 & m & 0 & -mz_g & 0 & mx_g \\ 0 & 0 & m & my_g & -mx_g & 0 \\ 0 & -mz_g & my_g & I^b_{yy} + I^b_{zz} & -I^b_{yx} & -I^b_{zx} \\ mz_g & 0 & -mx_g & -I^b_{xy} & I^b_{zz} + I^b_{xx} & -I^b_{zy} \\ -my_g & mx_g & 0 & -I^b_{xz} & -I^b_{yz} & I^b_{xx} + I^b_{yy} \end{bmatrix} \tag{5.2}$$

where m is the total mass of the system, the mass moments of inertia and the centre of gravity are computed with respect to the flotation centre. The moments of inertia are computed for the different elements assuming an homogeneous material distribution. The principal axis theorem is used to translate them to the centre of flotation. The RNA is approximated as a cylinder, using as characteristic lengths the size of the nacelle, due to the light weight of the blades.

5.2. Decay tests and natural frequency identification

A decay test of the system was performed in the reduced-order model to verify the system formulation, match the natural frequencies, and analyse the damping. Figure 5.1 shows the system decay for surge, sway, and heave motions for initial system displacements of 0.2 meters individually in each direction. There is much higher system damping in surge and sway than the respective rotating motions, pitch and roll. This can be seen in the relative decrease in motion amplitude in the time series, and the strong coupled frequency response in the surge and sway PSD plots from the pitch and roll motions. This can also be seen clearly in Figure 5.2, where the surge and sway motions look like the pitch and roll response in the decay test and their respective response frequency is only at the pitch and roll frequencies.

The heave decay is almost non-existent, however, this is likely related to the formation of the radiation damping matrix, which will under-account for the hydrodynamic damping contribution of the heave plates given the modeling only considers horizontal hydrodynamic forcing.

5.3. Response to wind and waves

The system's simulated response to wind and wave forcing shows some design flaws for the given turbine and testing conditions. In particular, the lack of mooring pitch stiffness apparent in the system response characteristics. Figure 5.3 shows the response to a steady 5 m/s wind and no wave forcing given the turbine's measured thrust curve. The system is very slightly unstable, however this is likely due to underrepresented hydrodynamic damping in the model and is not expected during the testing. The large mean pitch angle of 30.5 degrees is an undesirable result. The model assumes small angles, so any pitch angle above 10 degrees is inaccurate but the takeaway does not change that the system's pitch stiffness is too low.

The wave-only forcing response to regular linear waves is shown in Figure 5.4 and Figure 5.5. The two plots show completely difference character, which is due in large part to the implementation of hydrodynamic forcing in the modeling. The Morison equation is used for the hydrodynamic forcing, and the floater is approximated to 3 cylinders in the flow. The second two cylinders are forced out of phase with the first cylinder, assuming that the waves approach head-on. Therefore, the the surge response is significantly higher for the 5-second wave period rather than the 8-second wave period because of the phase difference of the forcing between the two cases. However, the pitch response of the 8-second wave period is much higher. Both show some lingering transience in the time series, demonstrating the slow decay of the pitch motion that is modeled.

There are significant limitations to using the Morison equation for hydrodynamic forces, but this was necessitated by time and resources available. The Morison equation is applied ignoring diffraction radiation from the waves interaction with the floater, which will impact the forcing in particular on the rear two cylinders. Additionally, the Morison equation is best applied to a cylinder that can be approximated as an infinitely long cylinder: the further away from this assumption the reality is, the less accurate the results. In this case, the submerged depth of the floating cylinders is 0.27 m, where their diameter is 0.2 m. This means that the Morison equation is likely a poorer approximation than desired for the magnitude of forcing. Another limitation is the use of the infinity damping and added mass matrices. The added mass and damping are frequency dependent for lower frequencies of forcing, which is not accounted for in the model Figure 3.11. Therefore, the results may not specifically present the frequency-dependent response of the system.

However, general conclusions about there being a frequency dependence in the system's response to hydrodynamic forcing which need to be tested for in the model's future design and validation is a valuable result. Additionally, there is a further illustration of the limitation of using a single mooring connection point with a loose catenary system, which is also a requirement specifically derived for the competition testing conditions.

The system response to wind and wave forcing together is shown in Figure 5.6. The interaction of wind and wave forcing as applied dampens the system's surge oscillation response from the wave forcing but still includes the same magnitude of the pitch oscillation from the same standalone wave forcing case in Figure 5.4, around the mean value of the pitch in the standalone wind forcing case in Figure 5.3.

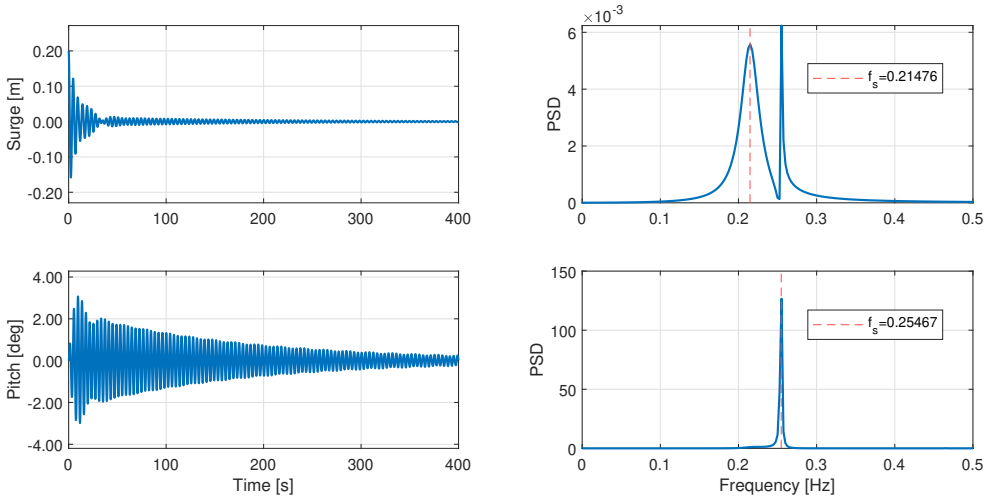

(a) Surge decay from 0.2 m initial displacement.

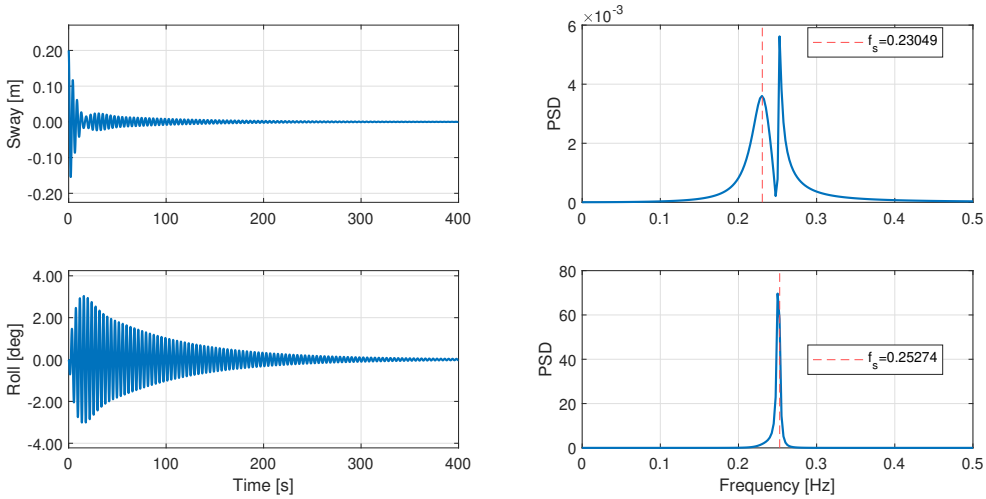

(b) Sway decay from 0.2 m initial displacement.

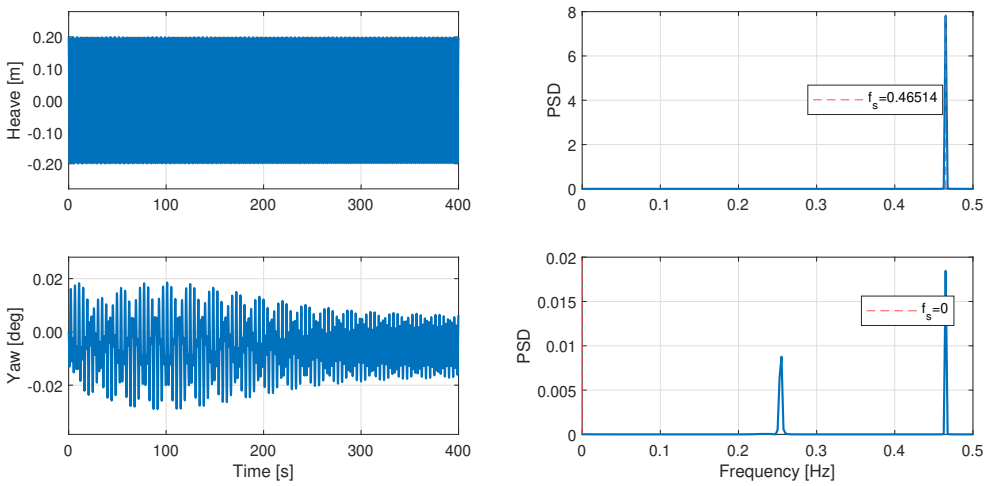

(c) Heave decay from 0.2 m initial displacement.

Figure 5.1: System decay response to initial translational displacements.

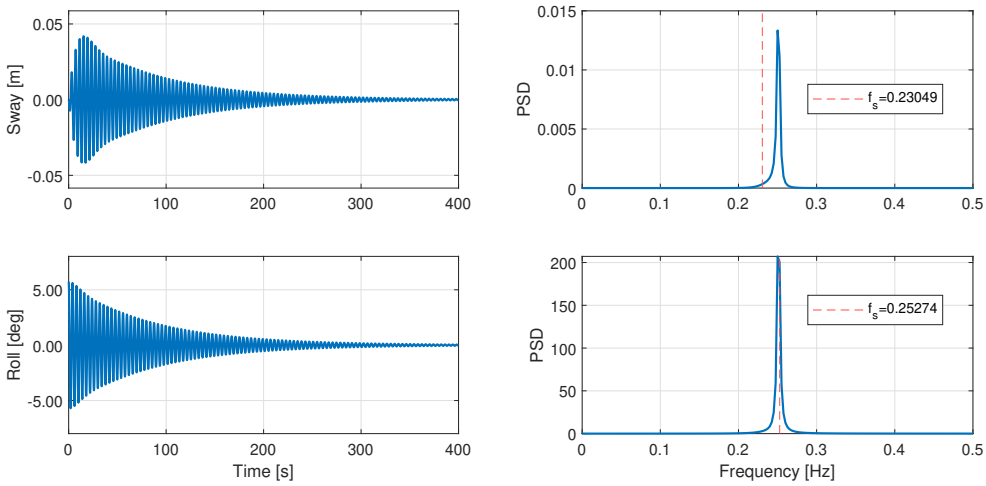

(a) Roll decay from 0.1 rad initial displacement.

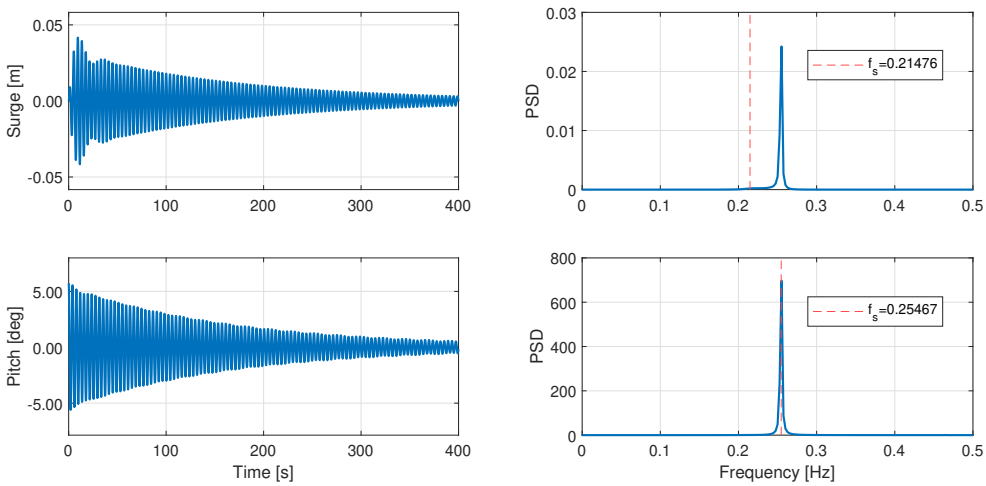

(b) Pitch decay from 0.1 rad initial displacement.

Figure 5.2: System decay response to initial rotational displacements.

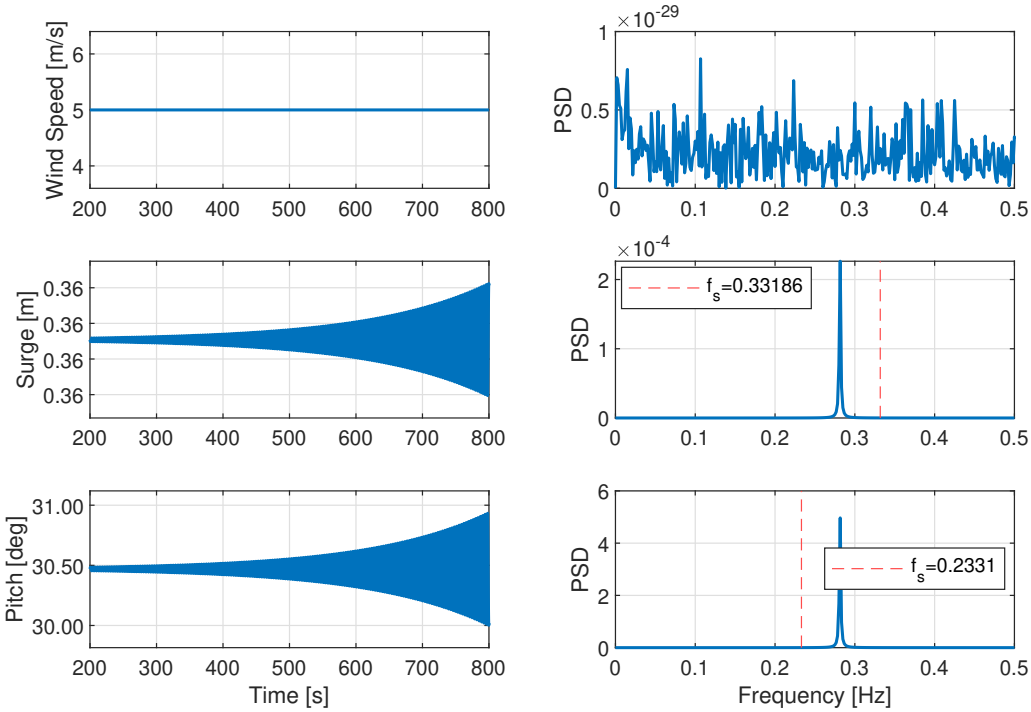

Figure 5.3: System response to steady 5 m/s wind forcing.

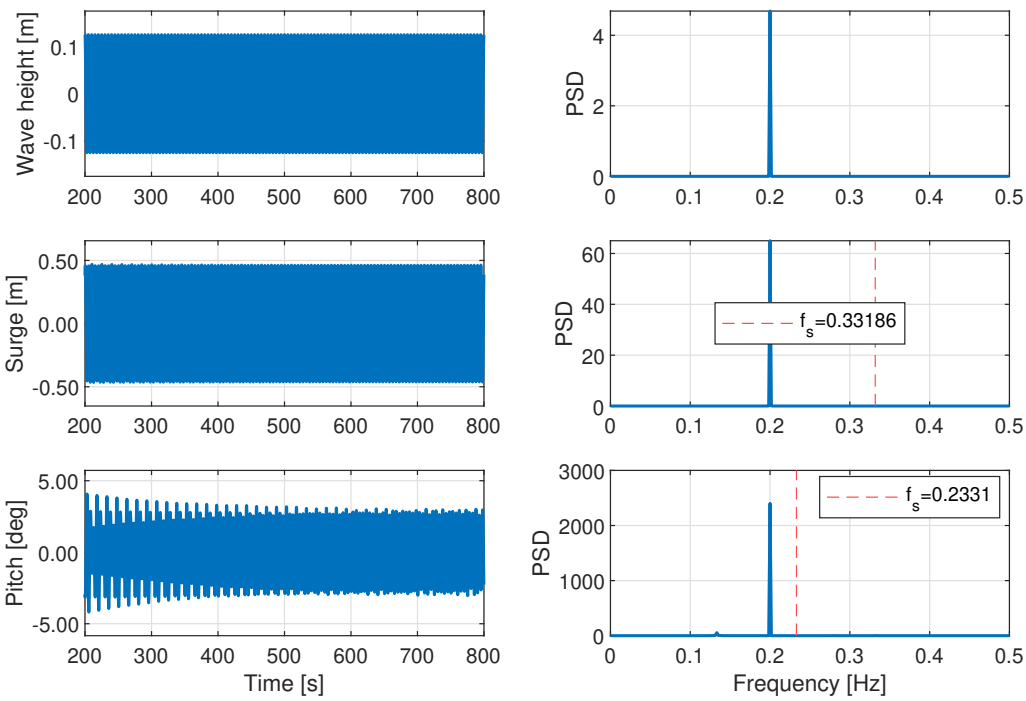

Figure 5.4: System response to regular linear wave forcing where $T_p = 5$ s and $H_s = 0.25$ m.

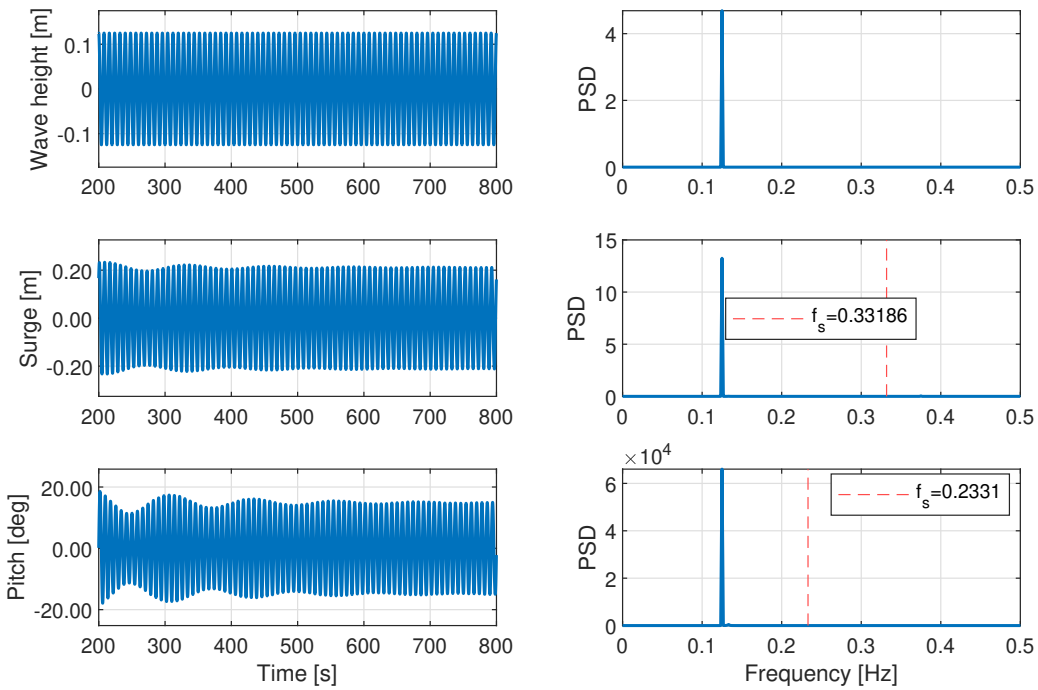

Figure 5.5: System response to regular linear wave forcing where $T_p = 8$ s and $H_s = 0.25$ m.

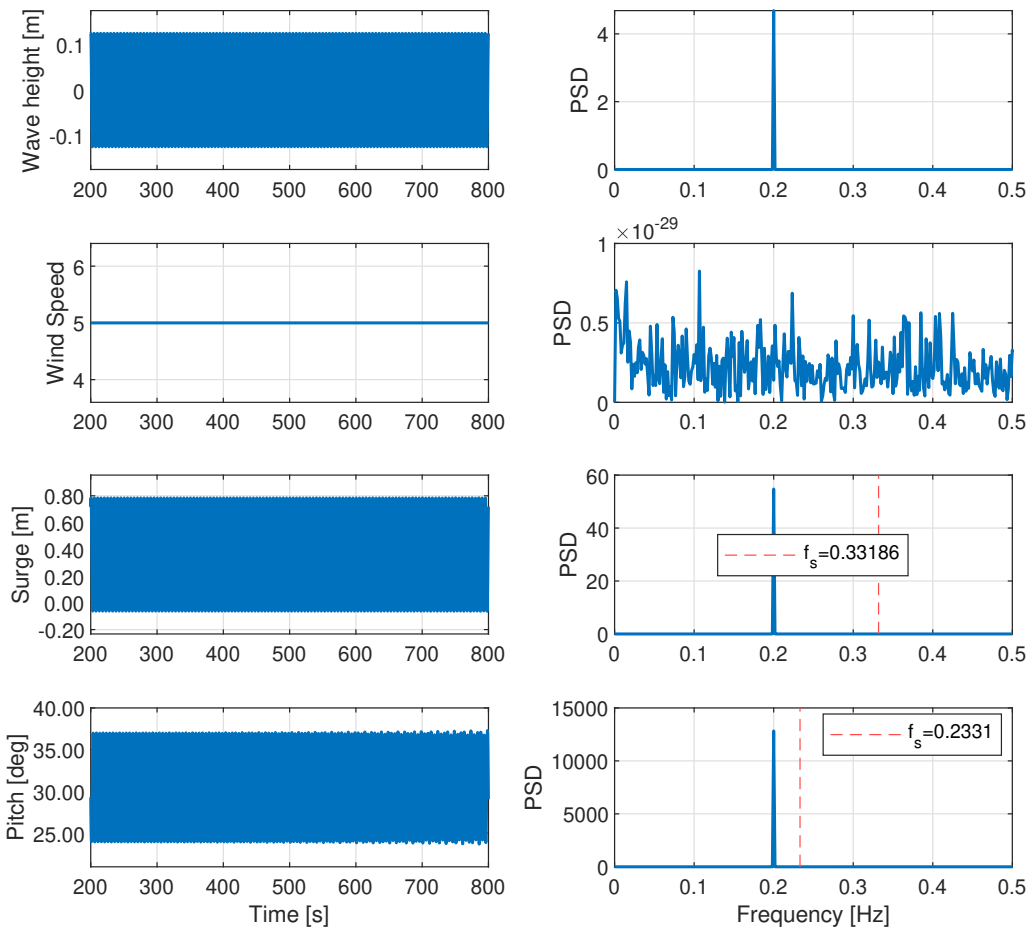

Figure 5.6: System response to steady wind forcing at 5 m/s and regular linear wave forcing where $T_p = 5$ s and $H_s = 0.25$ m.

6

Manufacturing process

The manufacturing of the scaled version of the floater was carried with modularity, and ease of commissioning and decommissioning in mind, as will be presented in this chapter. In section 6.1, the design decision taken in the conception of the floating platform will be discussed, and the main components of the floater will be presented. In section 6.2, the focus will be on the mooring lines and anchor, and the planned commissioning and decommissioning procedure.

6.1. Floating platform elements

Following the hydrodynamic design and analysis discussed in chapter 3, a design with numerous constraints was to be manufactured. Those constraints were namely related to a sufficiently wide floater foot-print and high draft to enhance floater stability, and a sufficiently tall tower to extract as much power from the wind.

The initial manufacturing plan for the floating platform is shown in Figure 6.1. In this diagram the mooring line connection points are not depicted. The floater structure can be categorised in four distinct parts:

- **Main frame |** This non-buoyant structure can be understood as the skeleton of the floater. It includes the wind turbine tower, the cross-members between buoys and the vertical members onto which the buoys are attached. This main frame is planned to be manufactured mainly from steel for its stiffness and availability in most hardware stores. This main structure is meant to be the backbone of the floater, onto which the remaining components such as buoys, heave plates, and mooring lines can be conveniently connected. The fact that this structure does not need to be buoyant allows to connect those additional components without the need for watertight joints on the main frame. Furthermore, the configuration of the main frame, with vertical member made out of pipe sections, and cross-members as threaded rods (c.f. Figure 6.2), allows to conveniently disassemble the frame for transportation. Besides, the vertical members of the main frame allow space to connect around them more than one buoy, hence allowing flexibility in the design. One of the vertical member will extend further to act as the wind turbine tower as well.
- **Buoys |** The buoys are made out of PVC pipe sections, sealed by caps on both ends, to make them watertight, and thus buoyant. The top cap is meant to be a threaded cap (c.f. Figure 6.2), for two main reason: first, to allow for inspection of the joints inside the buoys, and secondly to add ballast inside the tanks and lower the draft of the floater, if need be. The buoys are connected to the main frame with pipe collars, or also called pipe wall mounts (c.f. Figure 6.2), to allow for ease of assembly. In fact, the height at which the buoy is mounted onto the floater can quickly be adjusted.
- **Heave plates |** The heave plates are attached to the main frame, at the bottom of its vertical members. The material used for those plates is still under consideration, but it shall be relatively easily cut down to size and stiff enough to resist the mass of the water that will act on it.
- **Mooring lines attachment point |** Even though not shown in the diagram, the mooring lines will be connected to the floater at the base of the vertical members of the main frame, at the center of the heave plates.

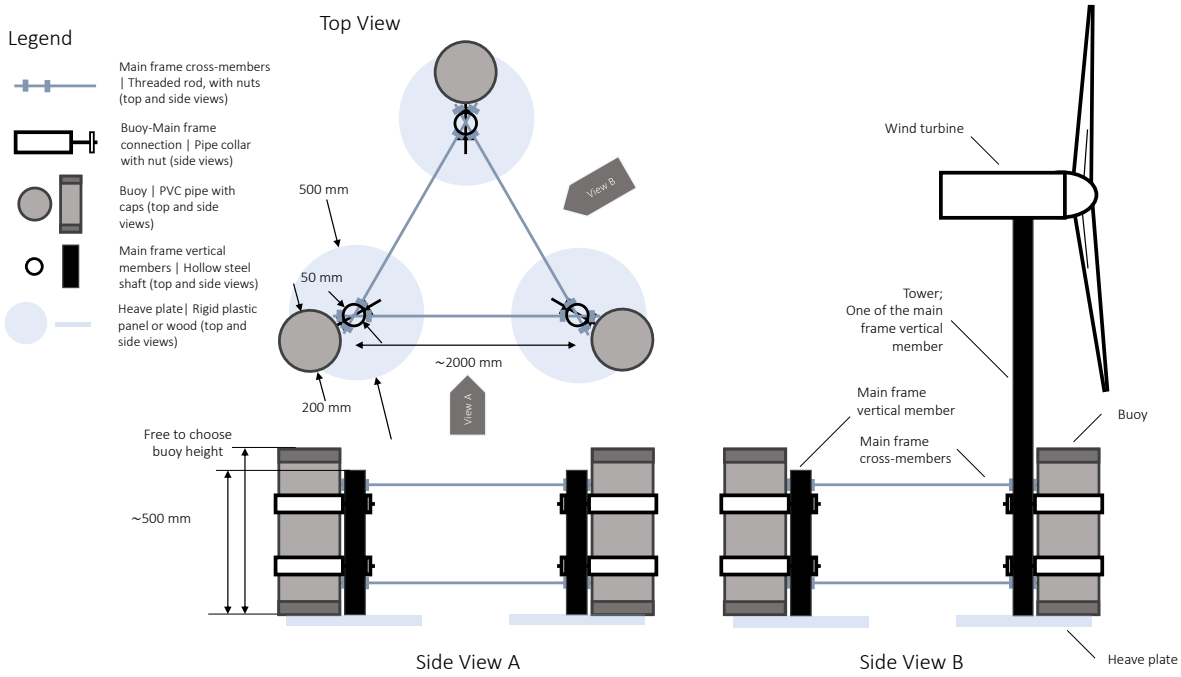

Figure 6.1: Top and side views of the initial manufacturing concept

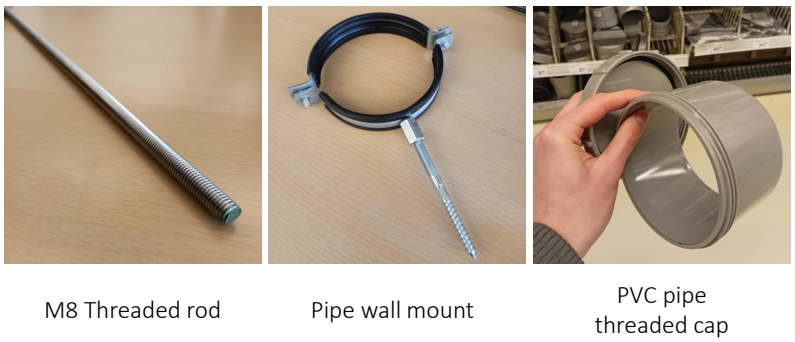

Figure 6.2: Key components of the initial manufacturing concept

For the present design concept, several limitations are found based on the availability of the components in hardware stores and workshops accessible to the team. These are listed in Table 6.1. The main limitations are the length of the main frame cross-members, and on the diameter of the buoys. In fact, the threaded rods that are to be used for the cross-members can be found in regular hardware stores length of maximum 2 m, hence constraining the radial dimension of the floater. Besides, the diameter of the buoys is constrained by the dimensions of PVC pipes that can be readily available in hardware stores, which are usually limited to diameters of 125 mm.

6.2. Mooring Lines and Anchors

The mooring lines were previously design to be catenary, as discussed in section 4.1. Steel chains available in hardware store will be used as mooring line, which will run from each vertical member of the main frame, away from the floater. To resist the lateral motion of the end of the mooring lines, the anchors considered are driven stakes as discussed in section 4.4 that will be driven in the sea bed. To ease decommissioning, a small buoy will be tethered to the anchor. In fact, having a buoy float at the surface of the sea, above each anchor, will assist in locating the anchor and help in pulling it out of the sea bed upon decommissioning.

Table 6.1: Floating platform element parameters and constraints

Element	Parameter	Symbol	Reference value	Available range
Cylindrical buoys	Diameter	D_b	0.2 m	$0.07, 0.08, 0.11, 0.125, 0.2$ m
	Height	H_b	0.5 m	≤ 2 m
	Thickness	t_b	0.005 m	$0.001 - 0.005$ m
	Material (Density)	-, (ρ_b)	PVC, 1450 kg/m^3	NA
Main frame cross-members	Diameter	D_{fr}	0.008 m	$0.005 - 0.010$ m
	Length	L_{fr}	1.3 m	$1.0 - 1.9$ m
	Material (Density)	-, (ρ_{fr})	Steel (8000 kg/m^3)	NA
Main frame vertical members	Diameter	D_{hs}	0.05 m	$0.02 - 0.10$ m
	Height	H_{hs}	0.5 m	≤ 1 m
	Thickness	t_{hs}	Fill thicknes	Fill thickness
	Material (Density)	-, (ρ_{hs})	Steel (8000 kg/m^3)	NA
Heave plates	Diameter	D_{hp}	0.4 m	$0.025 - 0.5$ m
	Thickness	t_{hp}	0.001 m	TBD
	Material (Density)	-, (ρ_{hp})	Steel (8000 kg/m^3)	Plastic corrugate, (1450 kg/m^3)

7

Concept scalability and financial analysis

In this section, we will discuss how the existing design can be scaled to a real-life usable scale.

7.1. Criteria for scaled design

The design is scaled to work with the DTU 10 MW reference turbine [6]. This turbine has sufficient data regarding thrust, while being of a similar scale to the largest turbines being installed at this moment in time. It is assumed that the same criteria hold as in the competition. Therefore, the goal is to design a floater that maximises power production, structural stability, and foundational stability, and minimises costs related to fabrication, installation, and operation.

An example floater is set as seen in Figure 7.1, with buoys 80m apart and the DTU 10 MW turbine perched atop. A discussion will be held of the pros and cons of such a design, as well as points for further development. Table 7.1 has an overview of some estimated dimensions, forces, and masses of the structure.

Figure 7.1: Floater upscaled for the DTU 10 MW reference turbine

L_{buoy} [m]	H_{buoy} [m]	$z_{draft,noturb}$ [m]	$z_{draft,ops}$ [m]	M_{float}[tons]	M_{turb}[tons]	$T_{turb,rated}$[MN]
80m	51	6.99	11.01	2071	1280	1.53

Table 7.1: Floater and DTU 10 MW reference turbine specifications [6]

Here, L_{buoy} is the inter-buoy distance, H_{buoy} is the buoy height, $z_{draft,noturb}$ is the draft without a turbine installed, $z_{draft,ops}$ is the draft with turbine, M_{float} is the mass of the floater, M_{turb} is the mass of the turbine, and $T_{turb,rated}$ is the thrust of the turbine. It must be noted that the floater mass is an initial estimate, and only includes the mass of major steel elements, not bolted connections or ancillary infrastructure.

7.2. Manufacturing and Materials

At full scale, we must consider how to integrate floater manufacturing into existing shipyards and supply chains. This is to reduce costs linked to developing new shipyards capable of handling a floater with a large draft and size. With buoys 80 metres apart, there are only a handful of dry docks and shipyards available worldwide with the facilities to produce such a design [7]. Most of these are located in locations such as France, Germany, and China, where potential for floating wind is high. This leaves large parts of the world, such as Africa and the Americas, where there is insufficient existing infrastructure to produce floating platforms of such scale. It becomes important then that the floater is highly modular, and can be assembled from common materials.

The floater can be built using standard steel for ships, allowing for easier construction by existing shipyards and production locations. The supply of steel to locations that have no existing shipbuilding industry remains an issue, but it would be expected that any large quantity of construction material would cause these issues. The connections between floater and its elements would be bolted wherever possible. This allows for easier commissioning and decommissioning, especially in areas with limited prior shipbuilding expertise.

7.3. Structural considerations

The loads on the floater will be significantly higher than for the scale model, requiring a overhaul of the structure. Comparing the rated thrust data from Table 7.1 and the thrust curve of the scaled turbine from Figure 2.5, it can be noted that they are roughly a factor 10^4 separated. Considering wave and fatigue loads, it will be required to have thicker, rigid connections between the turbine, buoys, and spars. Welding the structure would allow for a larger stiffness in the connections, and a reduction in material use and costs. On the other hand, it would require a much larger shipyard to produce in, which is not desirable for the production considerations outlined in section 7.2.

7.4. Mooring considerations

The scale-model floater has to deal with highly variable ocean depth and waves. Design choices for the scale model have been made with this in mind. It is expected that a full-scale model would not suffer from such a large variability in ocean depth. While the absolute change of 1-2 metres of tidal range may remain the same, the water depth would be much larger, around 80 metres. Here, it becomes more important that the mooring is easy to install, maintain, and decommission. A pivot buoy system could work well on a full-scale model. The smaller variation in water depth would put a small load on the bearing, and the wind/wave misalignment is expected to be much larger in deeper water. As downside, any moving pivot would be subject to heavy corrosion, leading to rising maintenance costs. In areas with a low misalignment, the pivot can be excluded to improve weight and maintenance.

For mooring the floater to the seabed, a likely choice would be a TLP or taught cable system with a suction bucket. This would allow for a small mooring footprint of the floater, optimising it for use in offshore wind arrays. While a suction bucket has a large influence on the seabed, it has less influence than a drag anchor and catenary system. Taught mooring was excluded from the scale-model analysis as the large water depth change made modelling of line stiffness difficult, but in deep water with a relatively smaller stiffness change, it becomes a better option than catenary mooring.

7.5. Operations and maintenance considerations

Although the main costs originate from the initial capital expenditure (CAPEX), additional costs occur through the lifetime of the floating wind turbine due to the operations and maintenance (O&M).

Some of the most important ones are the maintenance and repair costs, monitoring and control of the WTG, personnel costs, or grid connection, amongst others.

The maintenance and repair of a floating wind turbine poses the main difference, when compared to traditional bottom-fixed wind turbines. On one hand, the installation in deeper seas leads to inherently rougher conditions, additional fuel costs for vessels to reach the wind turbine (wind farm) and higher probability of damage or malfunction of the WTG. Additionally, the motions of the platform lead to accessibility and workability limits. To reduce the latter, increase in the damping of the motions by means of the design can be considered, however the platform design tends to be optimised considering mainly (or only) the operation, loads and power production. On the other hand, the accessibility can be accounted for by means of adding access points to the floater. The reason behind it is the significant impact of the wave direction in the accessibility limits of a floating platform, as it is studied in [8]. Adding ladders in the back vertices of the floater can increase the accessibility, specially for sites where there is not a clear predominant wave heading.

7.6. Energy and Export Infrastructure

Current generation wind farms all use undersea cables to export power. However, Power-to-X is currently being researched as an alternative. This section will consider exporting of energy from the floating platform.

Power connection to any mainline grid would need to be transformed on-site. Transformers could be placed on some or all floating wind turbines, although this would require multiple designs to be implemented, increasing a project's complexity. Prefarably, the transformer would be on its independent platform, either bottom-fixed or floating, depending on water depth and site conditions.

Power Transfer cables within the wind farm would need to be submerged deep enough to allow maintenance ships to pass through. They would also need to be flexible enough to allow for movement of floating platforms. In the case of a Pivot Buoy design, it is important that the power cable does not interfere with the mooring cables as well. It may be necessary to connect the power cable to the base of the pivot joint, adding extra complexity but negating the risk of the power cable getting tangled. Connecting the power cable above water would greatly improve maintenance and installation, but can lead to the cable being wrapped around the mooring during floater rotation. A solution to this would be to have the power be connected to a moving ring, though this brings extra engineering difficulty with it.

For Power-to-X, it would be unwise to have floater-based hydrogen or methanol production. Developing a safe export pipe for such mediums is considered difficult, and should they fail the potential for damage to structures and the environment may potentially be high, depending on the synthesised material produced. Relying on ship-transport is also undesirable, as in bad weather this may not be able to happen for weeks at a time. A central point would be desirable for Power-to-X applications, though this would also have to be a floating platform due to water depths. This could be in the form of a ship with production and storage infrastructure on board, allowing it to be moored on-site to receive power from the turbines. Indeed, old LNG tankers or bulk/oil carriers might be converted to this function at a relatively low price compared to a ground-up vessel

Depending on local climate conditions, solar panels or tidal energy may be connected to floating platforms to provide extra power to export. Arrays of floating platforms could furthermore allow for staging points for further undersea infrastructure installation, such as fibre cables. These ideas however are merely speculative, and do not have any data to back up their desirability or feasibility.

7.7. Expected Construction and Operating Costs

While data is not readily available, some assumptions can be made on the costs a floating wind platform may incur. From Mhyr et. el. (2014) [9] we can find some data for floater finances. From this, and for the data in Table 7.1, assumptions can be made for floater complexity, performance, and costs. For the analysis, it is assumed 10Mw turbines will be used, with a wind farm of 200MW in size. This yields 20 floating platforms. The data for this analysis is compiled in Table 7.2.

Individual Floater Costs			
Floater Material cost [€]	2.07E+06	Anchor weight [tons]	140
Manufacturing Complexity Factor Low	1.8	Anchor Complexity Factor	10.25
Manufacturing Complexity Factor High	3	Anchor count	1
Manufacturing Cost Low [€]	3.73E+06	Anchor cost [€]	1.43E+06
Manufacturing Cost High [€]	1.12E+07	Mooring Line Length [m]	60
Wind Turbine Cost [€]	8.00E+06	Mooring Line Count	9
Structure Total Cost Lower Bound [€]	1.38E+07	Mooring Line Cost [€]	1.35E+05
Structure Total Cost Upper Bound [€]	2.13E+07	**Mooring Total [€]**	1570000

Wind Farm costs		**Profit**	
Farm rated output	2.00E+08	Energy selling Price (€/ kwh)	0.025
Number of Floaters	2.00E+01	Capacity factor lower bound	0.5
Internal Power Cable cost [€]	7.00E+06	Capacity factor upper bound	0.8
Transformer cost [€]	1.61E+08	Turbine Lifetime (years)	20
External cable costs [€]	2.40E+07	**Profit Low [€]**	4.38E+08
Fixed yearly O&M costs farm [€]	4766000	**Profit high [€]**	7.01E+08
Farm total lower bound [€]	5.95E+08	**Net Profit Low [€]**	-3.06E+08
Farm total upper bound [€]	7.44E+08	**Net Profit High [€]**	1.06E+08

Table 7.2: Financial overview for a 200MW reference wind farm

A number of comments can be made about the table. Starting with the floater material and manufacturing costs, these can be higher or lower depending on the complexity cost. The low factor is taken to be a bit lower than the WindFloat turbine data from [9], this refers to the floater without a pivot-buoy design. With a pivot buoy design, the complexity increases significantly, and is expected to be much higher. The price of a 10MW wind turbine is assumed to be roughly 8 million Euro.

The Mooring line data is taken from data for SWAY and TLWT - taut [9]. The mooring line length depends on water depth, and the chains are assumed here to be 60 metres long as a lower bound. Chain count and length has a reasonable influence on the mooring cost.

Concerning the capacity factors, 0.5 is similar to current offshore wind farms, while 0.8 is an optimistic scenario for floating wind. The lowest net profit assumes a more expensive pivot buoy structure, with a low capacity factor, where the highest profit is for the high capacity factor and simpler structure. The total extra cost of choosing a pivot buoy over a conventional design is around 26%. Even with the highest profit case, no net profit will ever be made at current energy prices for a pivot buoy. A conventional structure requires a capacity factor of at least 0.68 to make a profit.

A number of cost reductions can be considered to improve both structure's use case. First, the pivot buoy can be considered. The turbine may be cheaper without a bearing and an A-frame tower of reduced cost, at an estimate it may only cost 6 M€ instead of 8 M€. If the structure is simpler than expected, the complexity factor can be reduced to 2.5, and fewer mooring cables can be considered, 4 are assumed. This allows the pivot-buoy concept to turn a profit if the capacity factor is 0.8.

To turn a profit for a pivot buoy at a lower capacity factor of 0.5, the wind farm would need to be twice as large, with an installed capacity of 400MW. It will be assumed wind farm costs don't increase and the operation lifespan is increased to 25 years as well. The profit for a conventional system is over five times larger in this scenario compared to a pivot buoy, although to turn a profit at a capacity factor of 0.5, it would still require an increase to 300MW total installed capacity, and a lifespan of 25 years. The benefits of a pivot buoy at current technology levels are slim from a financial perspective, and a conventional system will also only produce benefits for larger farms and power outputs.

It must be noted this is an initial feasibility study based on scaling factors and fixed operating costs. Further analysis will be required to take into account more factors, such as installation/operational vessel deployment, decommissioning, and Power-to-X installations. Considering modern turbines are up to 15MW in capacity, the cost analysis must be carried out for larger turbines as well when the data becomes available.

8 Conclusion

The larger turbine as well as the more complicated wave conditions with misalignment, breaking waves, shoaling and tidal variations led to a greater design challenge for the floater this year.

Firstly, the wind turbine properties were measured using a load balance in the Wind AI Lab at TU Delft, and the thrust and torque were used as inputs for the reduced order models and simulations of the floater. The tower was designed to be a single steel cylinder.

A triangular design with three buoys was chosen for a floater design, but a double buoy was specifically chosen due to size constraints of available materials. A thorough hydrostatic analysis was performed for calculating the draft and investigating the stability of the floating platform which was considered for limitations over the final dimensions. The hydrodynamic analysis was done using the open-source software Salome to create the mesh and the potential-flow solver Nemoh for the derivation of the RAO of the floater. The results were also compared to OrcaWave for validation and were used as input to the reduced model simulations.

The simulated response of the testing-scale floater shows the limitations of a pivot buoy mooring connection when used with a loose catenary system, something that will need to be addressed in the full scale design. In particular, the pitch stiffness is too low. For a turbine with a peak thrust of 240 N, then the desired pitch stiffness to have a maximum pitch angle of 10 degrees is 1,375 Nm/rad, where the pivot buoy mooring system contributes 216.3 in the current design, showing a clear under-design. However, this neglects the wave forcing, which should contribute an opposing moment. The plan for the competition is to change the mooring fairlead attachment to a traditional three-point attachment to increase the pitch stiffness, as well as increase the mooring line weight. These are parameters more easily changed at the full-scale design, where the ability of the team members to install the floater at a beach is not a limiting design factor.

Scaling the floater is feasible. The capacity factor of any wind farm and the design of the floater are very important in determining total cost. A simple three-buoy semi-submersible floater with a TLP mooring system and suction-bucket anchoring will be profitable at a capacity factor of 0.5 provided the installed capacity is at least 300 MW, with a 25 year lifetime. More research is needed into factors that contribute to costs and losses in floating wind, especially at larget 15MW+ turbine scales. This way, Desirability and Viability of large-scale offshore floating farms can be considered.

A

Mooring stiffness terms

A.0.1. Single mooring line stiffness matrix, without transformations

$$
\begin{aligned}
K^P &= \begin{bmatrix} \frac{\partial T_H}{\partial l} & \frac{\partial T_H}{\partial h} \\ \frac{\partial T_V}{\partial l} & \frac{\partial T_V}{\partial h} \end{bmatrix} \\
\frac{\partial l}{\partial T_H} &= \frac{L_0}{EA} + \frac{1}{w}\left[\frac{-T_V}{\sqrt{T_H^2 + T_V^2}} + \text{arcsinh}\,\frac{T_V}{T_H}\right] \\
\frac{\partial l}{\partial T_V} &= \frac{1}{w}\left[\frac{T_H}{\sqrt{T_H^2 + T_V^2}} - 1\right] \\
\frac{\partial h}{partial T_H} &= \frac{\partial l}{\partial T_V} \\
\frac{\partial h}{\partial T_V} &= \frac{T_V}{w}\left[\frac{1}{\sqrt{T_H^2 + T_V^2}} + \frac{1}{EA}\right]
\end{aligned}
$$

A.0.2. Full mooring matrix terms, for a single mooring line

$$
\begin{aligned}
k_{11} &= K_{11}^P \cos^2\beta + \frac{T_H}{l}\sin^2\beta \\
k_{12} &= \sin\beta\cos\beta\left(K_{11}^P - \frac{T_H}{l}\right) \\
k_{13} &= \cos\beta K_{12}^P \\
k_{14} &= \cos\beta\left(K_{11}^P\frac{\partial l}{\partial\phi} + K_{12}^P\frac{\partial h}{\partial\phi}\right) - T_H\sin\beta\frac{\partial\beta}{\partial\phi} \\
k_{15} &= \cos\beta\left(K_{11}^P\frac{\partial l}{\partial\theta} + K_{12}^P\frac{\partial h}{\partial\theta}\right) - T_H\sin\beta\frac{\partial\beta}{\partial\theta} \\
k_{16} &= 0
\end{aligned}
$$

$$
\begin{aligned}
k_{21} &\equiv k_{12} \\
k_{22} &= \sin^2\beta K_{11}^P + \cos^2\beta \frac{T_H}{l} \\
k_{23} &= \sin\beta K_{12}^P \\
k_{24} &= \sin\beta \left(K_{11}^P \frac{\partial l}{\partial \phi} + K_{12}^P \frac{\partial h}{\partial \phi} \right) + T_H \cos\beta \frac{\partial \beta}{\partial \phi} \\
k_{25} &= \sin\beta \left(K_{11}^P \frac{\partial l}{\partial \theta} + K_{12}^P \frac{\partial h}{\partial \theta} \right) + T_H \cos\beta \frac{\partial \beta}{\partial \theta} \\
k_{26} &= 0
\end{aligned}
$$

$$
\begin{aligned}
k_{31} &\equiv k_{13} \\
k_{32} &\equiv k_{23} \\
k_{33} &= K_{22}^P \\
k_{34} &= k_{12}^P \frac{\partial l}{\partial \phi} + K_{22}^P \frac{\partial h}{\partial \phi} \\
k_{35} &= k_{21}^P \frac{\partial l}{\partial \theta} + K_{22}^P \frac{\partial h}{\partial \theta} \\
k_{36} &= 0
\end{aligned}
$$

$$
\begin{aligned}
k_{41} &= (Y_P - r_Y)\, k_{31} - (Z_P - r_Z)\, k_{21} \\
k_{42} &= (Y_P - r_Y)\, k_{32} - (Z_P - r_Z)\, k_{22} \\
k_{43} &= (Y_P - r_Y)\, k_{33} - (Z_P - r_Z)\, k_{23} \\
k_{44} &= (Y_P - r_Y)\, k_{34} - (Z_P - r_Z)\, k_{24} + T_V \frac{\partial Y_P}{\partial \phi} - T_H \sin\beta \frac{\partial Z_P}{\partial \phi} \\
k_{45} &= (Y_P - r_Y)\, k_{35} - (Z_P - r_Z)\, k_{25} + T_V \frac{\partial Y_P}{\partial \theta} - T_H \sin\beta \frac{\partial Z_P}{\partial \theta} \\
k_{46} &= 0
\end{aligned}
$$

$$
\begin{aligned}
k_{51} &= (Z_P - r_Z)\, k_{11} - (X_P - r_X)\, k_{31} \\
k_{52} &= (Z_P - r_Z)\, k_{12} - (X_P - r_X)\, k_{32} \\
k_{53} &= (Z_P - r_Z)\, k_{13} - (X_P - r_X)\, k_{33} \\
k_{54} &= (Z_P - r_Z)\, k_{14} - (X_P - r_X)\, k_{34} + T_H \cos\beta \frac{\partial Z_P}{\partial \phi} - T_V \frac{\partial X_P}{\partial \phi} \\
k_{55} &= (Z_P - r_Z)\, k_{15} - (X_P - r_X)\, k_{35} + T_H \cos\beta \frac{\partial Z_P}{\partial \theta} - T_V \frac{\partial X_P}{\partial \theta} \\
k_{56} &= 0
\end{aligned}
$$

$$k_{61} = 0$$
$$k_{62} = 0$$
$$k_{63} = 0$$
$$k_{64} = 0$$
$$k_{65} = 0$$
$$k_{66} = 0$$

Bibliography

[1] J. M. J. Journée and W. W. Massie, *Offshore Hydromechanics*, 1st ed. Delft University of Technology, 2001.

[2] Salome platform - the open-source platform for numerical simulation. [Online]. Available: https://www.salome-platform.org/

[3] (2022) Nemoh-presentation - lheea. [Online]. Available: https://lheea.ec-nantes.fr/research-impact/software-and-patents/nemoh-presentation

[4] R. Kurnia and G. Ducrozet, "Nemoh v3.0 user manual," 12 2022.

[5] M. K. Al-Solihat and M. Nahon, "Stiffness of slack and taut moorings," *Ships and Offshore Structures*, vol. 11, no. 8, pp. 890–904, 2016.

[6] C. Bak, F. Zahle, R. Bitsche, T. Kim, A. Yde, L. C. Henriksen, M. H. Hansen, J. P. A. A. Blasques, M. Gaunaa, A. Natarajan, and et al., "The dtu 10-mw reference wind turbine," Jun 2013. [Online]. Available: https://orbit.dtu.dk/en/publications/the-dtu-10-mw-reference-wind-turbine

[7] TrustedDocks. (2023) Largest dry docks. [Online]. Available: https://www.trusteddocks.com/record/top-dry-dock-in-length

[8] M. Martini, A. Jurado, R. Guanche, and I. Losada, "Probabilistic assessment of floating wind turbine access by catamaran vessel," *Energy Procedia*, vol. 94, pp. 249–260, 2016.

[9] A. Myhr, C. Bjerkseter, A. Ågotnes, and T. A. Nygaard, "Levelised cost of energy for offshore floating wind turbines in a life cycle perspective," *Renewable Energy*, vol. 66, p. 714–728, Jun 2014.